Title: A hybrid open-top light-sheet microscope for multi-scale imaging of cleared tissues

Authors: Adam K. Glaser[1*], Kevin W. Bishop[1,2], Lindsey A. Barner[1], Robert B. Serafin[1], and Jonathan T.C. Liu[1,2,3*]

[1] Department of Mechanical Engineering, University of Washington, Seattle, WA USA

[2] Department of Bioengineering, University of Washington, Seattle, WA USA

[3] Department of Pathology, University of Washington, Seattle, WA USA

[*]To whom correspondence should be addressed: akglaser@uw.edu and jonliu@uw.edu

One sentence summary: Glaser *et al.* describe a hybrid open-top light-sheet microscope to image cleared tissues at mesoscopic to sub-micron resolution and depths of up to 1 cm.

Abstract

Light-sheet microscopy has emerged as the preferred means for high-throughput volumetric imaging of cleared tissues. However, there is a need for a user-friendly system that can address diverse imaging applications with varied requirements in terms of resolution (mesoscopic to sub-micron), sample geometry (size, shape, and number), and compatibility with tissue-clearing protocols of different refractive indices. We present a hybrid system that combines a novel non-orthogonal dual-objective and conventional open-top light-sheet architecture for highly versatile multi-scale volumetric imaging.

Introduction

Recent advances in tissue-clearing protocols, which homogenize the refractive-index composition of tissues to reduce light scattering (i.e. promoting tissue transparency), have enabled deep optical access within intact tissues to yield new insights in many fields, including neuroscience, developmental biology, and anatomic pathology [1-9]. Although cleared tissues can be imaged using any optical approach, light-sheet microscopy has emerged as the preferred means for high-resolution volumetric imaging due to its unrivaled speed and optical efficiency (low photobleaching). As a result, a large and growing number of light-sheet microscopes have been developed by academic researchers and industry for cleared-tissue imaging (**Supplementary Tables 1 and 2**) [10-14]. While each system offers advantages, certain trade-offs are inevitable. For example, imaging chambers often constrain specimen size or thickness, objective lenses can be incompatible (optically and/or chemically) with various clearing protocols, and achievable resolution ranges are limited.

We have previously developed a number of open-top light-sheet (OTLS) microscopy systems that provide an ease-of-use similar to that of a flat-bed document scanner, enabling one or more specimens of arbitrary geometry to be imaged without lateral constraints up to a depth of several millimeters [15-17]. The OTLS architecture also offers the versatility to accommodate a wide range of potential accessory technologies, such as microfluidics, electrophysiology, and micro-dissection/aspiration. However, in terms of shortcomings, in addition to being somewhat limited in imaging depth (e.g. 5 mm deep for a recent system), these OTLS prototypes have been constrained to image at a fixed resolution (low to moderate) with relatively severe index-matching requirements for the specimen and specimen holder at higher numerical apertures (NA) (**Supplementary Figure 1**). Therefore, we set out to design a new OTLS microscope system that could serve as a versatile multi-scale imaging platform for a wide array of cleared-tissue imaging applications, with the ability to achieve a large imaging depth, resolution range, and insensitivity to index-mismatch (**Supplementary Figure 2**). In particular, since volumetric imaging speeds scale to the third power with respect to spatial resolution, we were motivated by the need for a system that could enable a hierarchical multi-scale imaging workflow, as is common with 2D microscopes containing a turret of objective lenses, to rapidly screen large volumes of tissue at lower resolution before interrogating localized regions of interest/ambiguity at higher resolution.

Our new hybrid system synergistically combines the advantages of a novel modified oblique-planar microscopy (OPM) architecture, which we refer to as a non-orthogonal dual-objective (NODO) configuration, with a conventional OTLS geometry, which we refer to as an orthogonal dual-objective (ODO) configuration. In terms of versatility, we demonstrate that this hybrid system is not only compatible with all clearing protocols, but unlike past OTLS systems, enables the combination of nearly any clearing reagent and specimen holder material with negligible degradation in imaging performance (**Supplementary Figure 3**). Tunable resolution is achieved over a range roughly corresponding to what is achieved by standard 2X to 40X objective lenses (NA = 0.025 to 0.70), enabling efficient hierarchical imaging workflows. Finally, the optomechanical design of the system imposes no lateral constraints on the specimen, enabling convenient imaging of multiple large specimens at a depth of up to 1 cm. In summary, our hybrid OTLS system offers an unprecedented balance of imaging specifications (resolution range and depth) and ease-of-use features (e.g. tolerance to index-mismatch and open-top sample-mounting) to address a wide range of biomedical applications.

Results

Our prior generations of OTLS microscopes featured an ODO architecture (similar to inverted light-sheet systems), in which the illumination and collection paths are each oriented at 45 deg with respect to the vertical axis (**Fig. 1a**) [15-21]. While these systems achieved low to moderate resolution (~1 μm), we sought to improve the resolving power of our new system to address the many applications that require sub-micron-scale imaging. However, there are two major challenges with the ODO architecture as one strives to improve spatial resolution: (1) High-NA objective lenses tend to have shorter working distances, which is exacerbated if the objective lenses are oriented at an oblique angle with respect to a specimen holder. This limits the imaging depth in thick specimens. (2) In the case of open-top systems, at high NAs, the quality of off-axis focused beams is severely degraded (aberrated) in the presence of minute refractive-index disparities between the cleared tissue, holder, and immersion medium [17, 18].

In order to achieve higher-resolution OTLS imaging, we considered the use of a non-orthogonal single-objective (NOSO) architecture (also known as OPM, SCAPE, and SOPi), that has gained popularity in recent years [22-29] (**Fig. 1b**). With NOSO systems, the illumination and collection beams share a single objective lens, in which a remote focus is used to re-image the non-orthogonal light sheet onto a flat detector array (camera chip). Orienting the objective lens in the normal direction (perpendicular) with respect to the specimen holder makes full use of the objective lens' working distance and dramatically reduces the system's sensitivity to refractive-index disparities. While the NOSO architecture mitigates the working-distance and index-mismatch limitations of ODO, there are several shortcomings of NOSO. In particular, since the illumination and collection paths share one objective lens, their NAs and crossing angle are limited and are also coupled such that axial and lateral resolution must trade off (**Supplementary Figure 4**). While this is less problematic for objective lenses with very high NAs (e.g., >1.0), such objective lenses exhibit a limited field of view (FOV) and short working distance, which are not ideal for multi-scale imaging of large cleared tissues (**Supplementary Figure 5**) [30]. Note that one of the advantages of NOSO is that it facilitates the use of a single mirror to scan and de-scan the illumination and collection paths for imaging live, dynamically changing specimens. However, this ability is less important for imaging fixed tissues, in which stage scanning is a viable alternative.

In order to achieve an optimal combination of resolution (axial and lateral), working distance, and insensitivity to index-mismatch, we developed the NODO architecture. By using the full NA of a vertically oriented objective lens for fluorescence collection, and a separate objective lens for non-orthogonal illumination (with the same remote-focus imaging strategy as NOSO), our NODO configuration maintains the working-distance and index-mismatch-insensitivity advantages of NOSO, while offering the improved imaging performance of a dual-objective lens system (**Fig. 1c**). In addition, since the use of a separate illumination objective lens increases the crossing angle of the two beams, it reduces the angle of the remote objective lens that is used to re-image the tilted light sheet. This enables standard off-the-shelf air objective lenses to be used as a remote objective lens rather than necessitating the use of specialized bespoke objective assemblies (**Supplementary Figure 6**) [26, 27]. Finally, by selecting a vertically oriented primary objective lens with optimal optomechanical specifications, and choosing a crossing angle of 45 deg, we add a separate collection arm for low-resolution OTLS imaging via an ODO architecture, in which a low-NA collection objective lens with a large field of view (FOV) enables rapid mesoscopic-resolution imaging (**Fig. 1d**).

The layout of our hybrid OTLS microscope is shown in **Fig 2a**, featuring three main objective lenses that are optimally selected to avoid geometric interference. All three objective lenses are positioned below the specimen, and are sealed into a monolithic imaging chamber through direct immersion or the use of a solid-immersion meniscus lens (SIMlens) (**Supplementary Figure 7**) [16]. This provides an unobstructed open top that enables laterally unconstrained imaging to a depth of 1 cm. Large or multiple specimens can be quickly mounted and dismounted via a modular magnetic holder, with light pressure from above to stabilize the specimens during imaging (**Supplementary Figure 8**). Finally, 3D imaging is achieved using a motorized XYZ stage and stage-scanned image acquisition. The optical layout is shown in **Fig. 2b**. Similar to NOSO, the NODO collection path re-images the non-orthogonal light sheet onto a camera using a remote focus whereas the ODO collection path is able to directly image the orthogonal light sheet onto a camera.

As described previously, the NODO architecture provides improved axial and lateral resolution compared to the NOSO architecture (**Figs. 2c-d**), and a ~100 fold improvement in index-mismatch tolerance compared to an ODO architecture with the same NA (**Figs. 2e**). To facilitate multi-scale imaging, the light sheet properties (i.e. width, thickness, and depth of focus) and overall magnification of the NODO and ODO imaging paths are tunable, providing either NA- or FOV-limited imaging (see **Supplementary Note 1** for discussion of these two imaging modes). In the current design, discrete magnifications are implemented at the extremes of each imaging path. The future addition of motorized zoom modules would allow our system to provide a nearly continuous resolution range of ~ 0.4 to 10 µm, corresponding to volumetric imaging speeds of ~ 0.3 mm^3 sec^{-1} to 3000 mm^3 sec^{-1} respectively (**Fig. 2f**). Detailed imaging specifications, including lateral and axial resolution at all set points, are shown in **Supplementary Table 3**. Finally, optical models and a photograph of our current hybrid OTLS microscope system are provided in **Supplementary Figures 9 – 15**.

Discussion

In comparison to existing academic and commercial light-sheet microscopy systems, our hybrid OTLS system provides significantly improved versatility and performance, as necessary to satisfy the diverse requirements of a growing number of cleared-tissue imaging applications. Our system is compatible with all clearing protocols, and unlike past OTLS systems, enables the combination of nearly any clearing reagent and specimen holder material. In addition, by combining a novel NODO configuration with a conventional ODO configuration, the system is capable of broad multi-scale imaging to enable efficient hierarchical imaging workflows from rapid mesoscopic surveys of large volumes to detailed interrogation of sub-micron features within localized regions of interest. Finally, the open-top geometry enables laterally unconstrained imaging up to a depth of 1 cm. Note that the physical layout of our hybrid system bears some resemblance to the light-sheet theta microscopy (LSTM) architecture, which employs dual-path illumination with a pair of off-axis objective lenses [11]. However, the NODO architecture, which forms one part of our multi-scale hybrid system, is >10X more light-efficient compared to LSTM with less trade-offs between light efficiency and axial resolution (see **Supplementary Note 2**).

Both the axial and lateral resolution of the hybrid OTLS system can be improved if needed. The axial resolution of the system can be enhanced by incorporating axial sweeping into the illumination optical path [13, 14, 31]. Unlike NOSO, our new NODO architecture allows the illumination NA to be increased substantially without necessitating a concomitant decrease in collection NA. Alternatively, with the 45 deg orientation of the two low-NA objective lenses in our system (one on either side of the NODO collection objective lens), it may also be possible to perform dual-sided illumination with fusion deconvolution to achieve NODO imaging with near-isotropic resolution (**Supplementary Figure 16**) [21]. Similarly, the lateral resolution of the system can be improved by increasing the collection NA of the multi-immersion objective lens. The current collection NA corresponds to an optical cone angle of ~28.9 deg, which is ~9 deg less than the ~37.9 deg mechanical bevel of the objective lens (**Supplementary Figure 17**). In theory, this gap can be reduced, increasing the collection NA (in air) from 0.483 to a maximum of 0.614. However, the optical cone angle cannot be increased beyond 40 – 45 deg for a hybrid NODO / ODO system, as this would not permit the ODO objective lenses from being positioned at 45 deg with respect to the vertical axis.

While our current design uses three separate objective lenses, it is worth noting the possibility of achieving similar multi-scale OTLS performance with a single objective lens

(NOSO configuration) with a large FOV, long working distance, and high NA (see **Supplementary Note 3** and **Supplementary Figure 18**). For example, the pupil of a single objective lens could be split into three separate regions, using the edges for illumination and ODO imaging, and only the center for NOSO imaging. However, this would require a customized objective lens with extraordinary specifications that could be prohibitively expensive to design and manufacture. Therefore, in summary, our hybrid OTLS design represents a practical means, with available optical components, of achieving an impressive balance of resolution, imaging depth, tolerance to index-mismatch, and multi-scale 3D imaging capabilities.

Online Methods

Hybrid open-top light-sheet microscope

Light-sheet-based imaging is achieved using three optical paths. The first obliquely illuminates the specimen with a light sheet at 45 deg relative to the vertical axis. The second is oriented vertically, enabling high-resolution collection of the light-sheet-generated fluorescence in a NODO configuration. Finally, the third is oriented at 90 deg relative to the illumination light sheet, enabling high-speed mesoscopic imaging in an ODO configuration. All three objective lenses are positioned below the specimen and are sealed into a custom-designed monolithic imaging chamber (machined by Hilltop Technologies). Stage-scanning is achieved by using an XY stage (MS2000, Applied Scientific Instrumentation) attached to two Z axis risers (LS50, Applied Scientific Instrumentation). The entire system is compact and fits on a portable 2’ x 3’ optical cart (POC001, Thorlabs).

Illumination optical path

The illumination optics were designed to allow for the light sheet properties (i.e. width, thickness, and depth of focus) to be adjusted. In addition, the optical path was designed to be compatible with the refractive-index, *n*, of all current clearing protocols (i.e., multi-immersion) and to minimize chromatic aberrations (i.e., the illumination focal length as a function of wavelength).

Illumination light is fiber-coupled into the system with a Gaussian numerical aperture (NA) of ~0.12 and collimated using an objective lens (RMS20X, Olympus). The beam diameter is then adjusted using a 4X variable beam expander (BE052-A, Thorlabs). This serves to adjust the overall NA of the light sheet. The variably expanded beam is then scanned using a pair of large-beam-diameter galvanometric scanning mirrors (GVS012, Thorlabs). One mirror is used to create a digitally scanned light sheet [32]. The other scanning mirror is used to align the light sheet with the focal plane of the NODO and ODO imaging paths. A pair of achromatic doublet lenses (AC508-75A and AC508-200A, Thorlabs) are then used to relay the scanned beam to the back focal plane of a 2X illumination objective lens with NA = 0.10 (TL2X-SAP, Thorlabs). Finally, the illumination light travels through a custom-fabricated solid immersion meniscus lens (SIMlens) (fabricated by BMV Optical) (**Supplementary Figure 7**) [16]. The SIMlens provides multi-immersion performance and prevents chromatic aberrations of the light sheet by minimizing refraction of the illumination rays as they transition from air into the immersion medium. In addition, since ray angles are preserved, the SIMlens increases the NA of the illumination light sheet by a factor of n. When combined, this optical design yields a light sheet with tunable NA (0.025 – 0.10 x n) and tunable width (0 – 11 mm / n) limited by the field of view (FOV) of the illumination objective lens. As with our past OTLS systems, the light sheet NA is tuned to provide a Rayleigh range that corresponds to 256 pixels on the detection camera. For the NODO imaging path, this corresponds to an axial re-focusing range of < 88 µm, which is well within the range of operation for an idealized objective lens, as specified by Botcherby et al. [22].

A digitally scanned light sheet was chosen over a cylindrical-lens approach (static light sheet), as achieving a high level of tunability for multi-scale imaging would be exceedingly difficult without the flexibility of the scanning mirror. Moreover, large scanning mirrors were selected to fill the back focal plane of the final illumination objective lens (i.e., to generate a higher NA light sheet). This was done in order to avoid having to significantly magnify the beam after the scanning mirrors, which would reduce the lateral scanning ability of the mirrors (i.e., constrain the maximum light-sheet width). In the current design, rotating the scanning mirror results in lateral scanning at a rate of ~0.60 mm per deg / n. The maximum desired light sheet width (i.e. lateral scanning range) is 11 mm, corresponding to a scanning angle of ~18 deg, which is within the designed maximum of the scanning mirrors (20 deg). A physical layout and ZEMAX model of the illumination optics are shown in **Supplementary Figure 9**.

NODO optical path

The NODO optical path of our system uses a multi-immersion objective lens (#54-12-8, Special Optics) with a long 1 cm working distance. This objective lens is compatible with all clearing protocols (n = 1.33 – 1.56) and provides a NA of 0.483 (in air) that scales with the index of the immersion medium (e.g., NA ~ 0.75 at n = 1.56). The lens is oriented in the normal (vertical) direction with respect to the specimen holder/interface and is therefore non-orthogonal to the light sheet. To image this non-orthogonal light sheet, we use a remote focus analogous to OPM and subsequent NOSO imaging techniques, with the multi-immersion objective lens serving as the primary objective lens (O1) [22, 23].

To minimize aberrations in the remote focus relay, the overall magnification from the specimen to the remote focus (air) should be equal to the refractive-index of the specimen, n. Given this requirement, the relay lenses and first remote objective lens (O2) must be carefully selected. For O2, a 20X objective lens is optimal, as a 10X or 40X objective lens would clip either the NA or FOV of our O1. Of the several companies which produce objective lenses, Zeiss and Leica were avoided due to the fact that chromatic aberrations are partially corrected in the tube lenses produced by these companies, which would complicate selection of the two relay tube lenses. Therefore, only objective lenses from Olympus and Nikon were considered, where 20X objective lenses from Olympus have a focal length of 9 mm, and 20X objective lenses from Nikon have a focal length of 10 mm. Factoring in the effective focal length of O1 (12.19 mm / n), the required relay lens magnification is ~1.219X for Nikon and ~1.354X for Olympus.

Well-corrected tube lenses are available with a limited selection of focal lengths (100, 165, 180, and 200 mm). Although custom tube lens assemblies are possible [27], we found that off-the-shelf 200-mm (Nikon Tube Lens #58-520, Edmund Optics) and 165-mm (TTL165-A, Thorlabs) tube lenses provide a magnification of ~1.212X, which matches the requirement for Nikon. Therefore, we decided to select a 20X Nikon objective lens for O2. To remotely correct for spherical aberrations introduced by the index-mismatch of the specimen holder, we narrowed our selection to only Nikon objective lenses offering a correction collar. This yielded two options, the CFI S Plan Fluor ELWD 20XC (NA = 0.45) with a correction collar for a cover glass of $t = 0 – 2$ mm, and CFI S Plan Fluor LWD 20XC (NA = 0.70) with a correction collar for a cover glass of $t = 0 – 1.8$ mm. As will be discussed in more detail, we selected the CFI S Plan Fluor ELWD 20XC, as our selection of the second (tilted) remote objective lens (O3) limits the effective NA to 0.45, although in an alternative design, the CFI S Plan Fluor LWD 20XC could be combined with a customized O3 to maintain the full 0.483 NA of our O1.

The goal of O3 is to maximize light collection when tilted at the angle required to orthogonally image a remote version of the oblique light sheet within the specimen. As mentioned previously, in a NOSO design, the light sheet angle would be limited by our chosen O1 to a maximum of 28.9 deg. This would require O3 to be tilted by at least 61.1 deg. At this extreme tilt angle, one way to prevent light loss is through a custom solid- or liquid-immersion objective lens [26, 27]. However, a benefit of our NODO design is that the crossing angle can be increased to 45 deg, which reduces the tilt of O3 to 45 deg. At this tilt angle, an objective lens with NA = 0.95 is able to capture light up to NA = 0.45. Therefore, for simplicity and ease-of-use, we opted to select a NA = 0.95 air objective lens for our O3.

In terms of selecting an optimal O3, we only considered objective lenses from Olympus and Nikon for the same reasons as mentioned previously. Both companies offer two types of objective lenses with NA = 0.95. These include 40X life-science objective lenses with a correction collar for cover-glass thicknesses ranging from $t = 0.11 – 0.23$ mm, and 50X metrology objective lenses for imaging with no cover glass. Although it would be possible to permanently align or adhere a cover glass to the 40X objective lenses, we decided to select the CF IC EPI Plan Apo 50X objective lens from Nikon for our O3 for simplicity and ease-of-use. When combined with a 100-mm tube lens (TTL100-A, Thorlabs), our NODO imaging path provides a total magnification of 25 x *n*. This yields a sampling rate of ~2.71 (slightly better than Nyquist) when using a sCMOS camera with pixels spaced by 6.5 μm (pco.edge 4.1, PCO Tech). Similarly, the FOV is ~ 0.53 mm / *n* (FOV = 0.40 - 0.34 mm when *n* = 1.33 – 1.56), which is not clipped by the 0.40 mm FOV of the 50X objective lens. The physical layout, ZEMAX model, and objective lens options for this NA-limited NODO imaging configuration are shown in **Supplementary Figure 10**.

While the above O3 selection provides NA-limited imaging, our O1 also provides a 1 mm FOV to enable FOV-limited imaging (with slightly worse resolution). To achieve this, we interchange O3 for a 20X objective lens with a matched 1 mm FOV. To minimize light loss, 20X objective lenses with the highest NA were considered. For both Olympus and Nikon, the upper limit is NA = 0.75 (although the recent UPLXAPO20X objective lens from Olympus offers NA = 0.80). While in a NOSO configuration, this selection of O3 would result in an effective NA ~ 0.12 x *n*, in our NODO configuration this results in an effective NA ~ 0.26 x *n*. This reduced effective NA (compared to the NA-limited case) closely matches Nyquist sampling of a 1 mm FOV with the same sCMOS chip as described earlier (with 2048 x 2048 pixels). To match parfocal lengths and thus enable a quick interchange of objective lenses, we selected the Nikon CFI Plan Apo Lambda 20X for our FOV-limited O3 objective lens. When paired with the same 100-mm tube lens (TTL100-A, Thorlabs), this provides a total magnification of 10 x *n*, which yields a near-Nyquist sampling rate of 2.02. The effective FOV is ~ 1.33 mm / *n* (FOV = 1.00 – 0.85 mm when *n* = 1.33 – 1.56), which is not clipped by the 1.00 mm FOV of the 20X objective lens (O3). The physical layout, ZEMAX model, and objective lens options for this

FOV-limited NODO imaging configuration are shown in **Supplementary Figure 11**. See **Supplementary Note 1** for more discussion of NA- versus FOV-limited imaging. Finally, as mentioned previously, an alternative design could use the CFI S Plan Fluor LWD 20XC and a customized O3 to use the full 0.483 NA of our O1 (see **Supplementary Note 4**).

ODO optical path

While the NODO imaging path is able to provide sub-micron resolution, the FOV of the multi-immersion objective lens is restricted to 1 mm, which is insufficient for fast mesoscopic imaging. This trade-off between NA and FOV is standard across all currently available microscope objective lenses (e.g., no current clearing-compatible lenses can simultaneously offer sub-micron resolution over a mesoscopic FOV) (**Supplementary Figure 4**) [30]. Therefore, in our hybrid system we achieve low-resolution imaging with a second independent ODO imaging path.

The ODO collection path uses the same objective lens as the illumination optical path (TL2X-SAP, Thorlabs). The objective lens is similarly used in conjunction with a SIMlens (fabricated by BMV Optical), which provides multi-immersion performance and prevents axial chromatic aberrations in the ODO imaging path. In addition, the SIMlens increases the NA of the collection path by a factor of n. This yields an effective NA = 0.10 x n.

NA-limited imaging is achieved using a tube lens with a 400 mm focal length (AC508-400-A, Thorlabs). This provides a magnification of 4 x n and an effective FOV of 3.3 mm / n, which corresponds to a near-Nyquist sampling rate of ~2.1 when using a sCMOS camera with a pixel spacing of 6.5 µm (pco.edge 4.1, PCO Tech, 2048 x 2048 pixels). FOV-limited imaging is achieved using a tube lens with a 100-mm focal length (TTL100-A). This provides a magnification of 1 x n and an effective FOV of 13.33 mm / n. Additionally, the beam is clipped behind the collection objective lens to 25% of the original diameter (corresponding to an effective NA of ~0.025 x *n*. This reduced effective NA provides a near-Nyquist sampling rate of 2.1 on the same sCMOS camera. The physical layouts and ZEMAX models of the ODO imaging configurations are shown in **Supplementary Figures 13 - 14**. See **Supplementary Note 1** for more discussion of NA- versus FOV-limited imaging.

Specimen holder design

To facilitate simple and robust mounting of specimens, a magnetic holder was designed using off-the-shelf Thorlabs parts. The back piece of a 60 mm cage plate (LCP90F-B) is attached to a custom machined adapter plate (machined by Hilltop Technologies), which is then attached to the XY stage (MS2000, Applied Scientific Instrumentation). The front piece of the 60-mm cage plate (LCP90F-F) is connected to a 1.5” diameter SM1.5 lens tube (SM1.5L10, Thorlabs) using a SM1.5 to SM2 threaded adapter (SM2A57, Thorlabs). The lens tube diameter is small enough to pass through the center of the 60 mm cage plate, and dip into the immersion chamber below the XY stage. Transparent specimen holder materials can then be interchanged and fixed to the bottom of the lens tube. Finally, a threaded SM2-to-SM1 smooth bore adapter (SM2A21, Thorlabs) can be threaded into the specimen holder, and a SM1 lens tube (SM1L15, Thorlabs) can be lowered down and locked with a set screw to lightly compress the specimen from above, stabilizing it during imaging. A schematic of the specimen holder is shown in **Supplementary Figure 8**.

Optical performance simulations

To calculate the axial and lateral resolution of the various system configurations, a custom simulation code was developed in Python. In short, the polar and azimuthal ray angles (spherical coordinate system) for a given NA across the pupil of O2 were calculated over a grid with a user-defined numerical resolution (default 256 x 256). The incident angle of these rays on a tilted O3 were then calculated, as shown in **Supplementary Figure 19** and described in [18]. Based on the acceptance NA of O3, the pupil plane was then clipped in 2D, yielding the final pupil pattern $P(k_x,k_y)$. Finally, the 3D point spread function (PSF) can be calculated as:

$$PSF(x,y,z) = \iint P(k_x,k_y)\, e^{2\pi i (k_x x + k_y y)} e^{2\pi i k_z (k_x,k_y) z} d_{k_x} d_{k_y}$$

where $k_z(k_x,k_y)$ acts to refocus the pupil pattern at varying axial positions [33]. Once the 3D PSFs were calculated, the full-width-half-maximum (FWHM) dimensions of the PSF were obtained along the three orthogonal directions (xyz). This code is available as **Supplementary Code**.

Index-mismatch simulations

To quantify the index-mismatch sensitivity of the various system configurations, simulations were performed using the optical ray-tracing software OpticStudio (ZEMAX). Blackbox files for the multi-immersion objective lens (#54-12-8, Special Optics) and 2X air objective lens (TL2X-SAP, Thorlabs) were used. The refractive-index of the immersion medium and specimen were set to $n = 1.46$. The optical path length of the specimen holder (Δn x t) was then varied. To assess the PSF, the real and imaginary components of the electric field were exported from ZEMAX, and input into a MATLAB (Mathworks) implementation of the beam propagation method (BPM) to obtain a full 3D PSF [34]. The Strehl ratio was evaluated by finding the maximum value of the 3D PSF.

Data Availability

The customized ZEMAX files are available as **Supplementary Data**.

Code Availability

The simulation codes used to model the lateral and axial resolution of the various microscope architectures is available on GitHub and as **Supplementary Code**.

Acknowledgements

We would like to thank Andrew York and Alfred Millet-Sikking for discussions regarding oblique planar microscopy, remote focus imaging, and alignment procedures. We would also like to thank Philip (Rusty) Nicovich for discussions on the NODO architecture, and Jon Daniels for discussions and his development of the multi-immersion objective lens. This work was funded in part by the National Institutes of Health (NIH) (K99 CA240681 (Glaser), R01CA175391 (Liu), Department of Defense (DoD) Prostate Cancer Research Program W81XWH-18-10358 (Liu), and National Science Foundation (NSF) Graduate Research Fellowships (Barner and Bishop).

Author Contributions

A.K.G. and J.T.C.L conceived of and designed the microscope system. A.K.G., K.W.B., and R.B.S. performed simulations of the microscope. A.K.G. fabricated the microscope system with help from L.A.B. All authors prepared the manuscript.

Competing Interests

A.K.G. and J.T.C.L. are co-founders and shareholders of Lightspeed Microscopy Inc.

Corresponding Author

Correspondence to Adam K. Glaser or Jonathan T.C. Liu

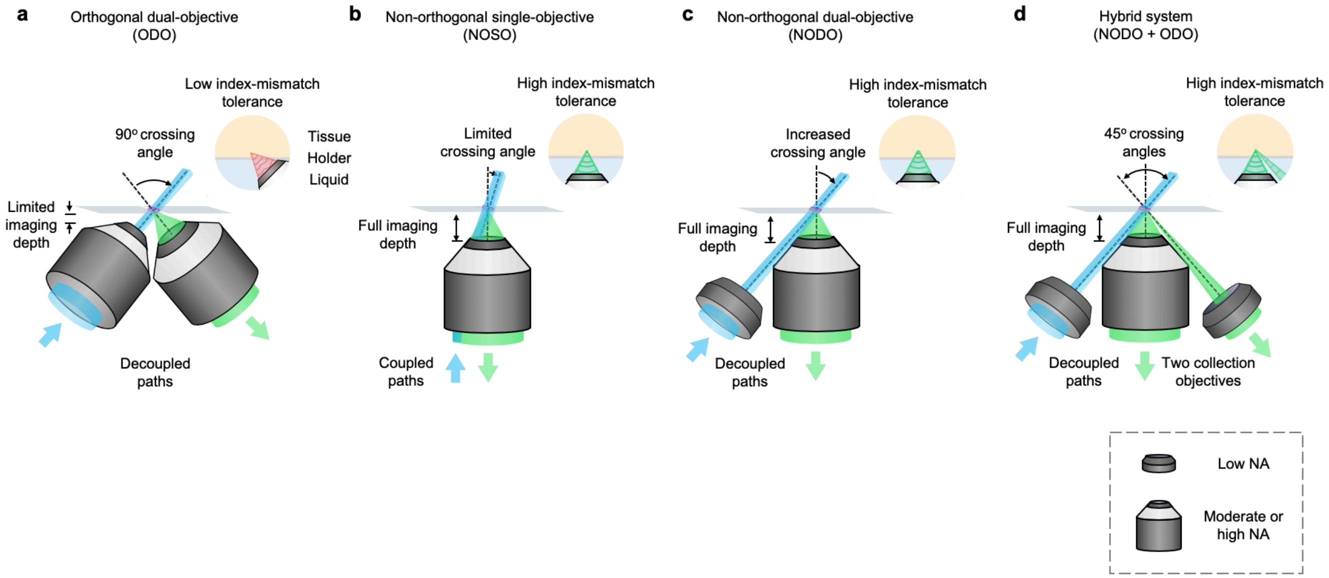

Fig. 1 | Comparison of open-top light-sheet architectures. (a) Initial open-top light-sheet (OTLS) microscopy systems used an orthogonal dual-objective (ODO) architecture, which decouples the illumination and collection paths but limits the imaging depth and increases sensitivity to index-mismatch between the tissue, holder, and immersion medium (liquid), especially if high-numerical-aperture (NA) objective lenses are used. Therefore, ODO systems are best suited for lower-resolution imaging (NA < 0.4). **(b)** The non-orthogonal single-objective (NOSO) architecture can be incorporated into an OTLS configuration by orienting the objective lens vertically, which maximizes the imaging depth of the system and greatly reduces sensitivity to index-mismatch. However, the use of a single objective lens limits the crossing angle between the two optical paths, resulting in severe trade-offs between lateral and axial resolution unless a high-NA objective lens is used. Therefore, NOSO systems are best suited for high-resolution imaging (NA > 1.0). **(c)** A non-orthogonal dual-objective (NODO) architecture operates similarly to a NOSO system, using a remote focus to re-image the tilted light sheet onto a flat camera chip. However, the light sheet is delivered using a second objective lens. This decouples the two optical paths and increases their crossing angle, which enables improved optical performance, especially when using a moderate-NA objective lens (NA = 0.4 – 0.9). **(d)** To enable multi-scale imaging, the hybrid OTLS system combines the strengths of a NODO and ODO system, providing an ideal balance of imaging performance (resolution), high tolerance to index-mismatch, and a large imaging depth to address a wide array of cleared-tissue microscopy applications.

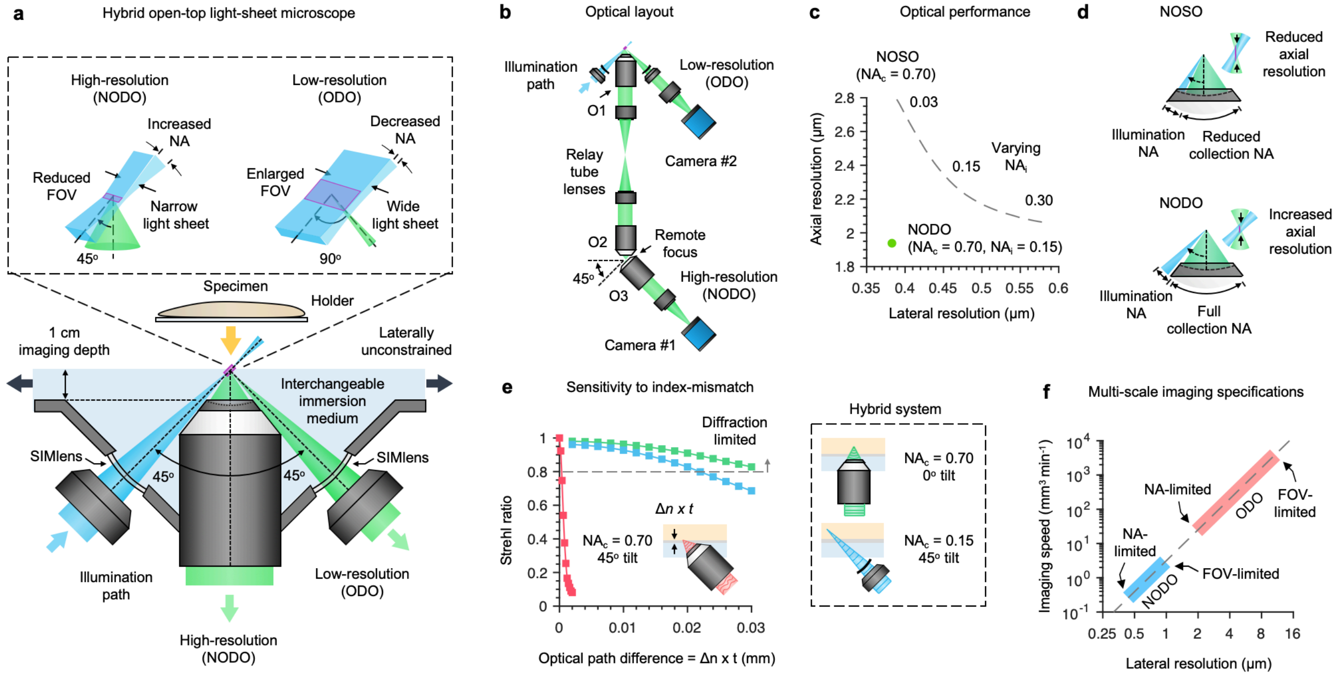

Fig. 2 | Hybrid open-top light-sheet (OTLS) microscope. (a) Light-sheet illumination (blue beam) is provided from an off-axis (45-deg) objective lens on the left. For high-resolution imaging, a vertically oriented objective lens images the fluorescence signal (green beam) from a small field of view (FOV) via a non-orthogonal dual-objective (NODO) configuration. For low-resolution imaging, a separate 45-deg off-axis objective lens (right side) images the fluorescence signal from a large FOV via an orthogonal dual-objective (ODO) configuration. The light-sheet illumination properties (thickness, width, depth of focus) are tuned for the NODO and ODO paths to enable multi-scale imaging. **(b)** The optical layout of the NODO configuration is inspired by a non-orthogonal single-objective (NOSO) light-sheet microscopy technique that has been gaining traction in recent years. Fluorescence is collected by the primary objective lens (O1) and is relayed to a remote focus using a pair of tube lenses and a second objective lens (O2). The final remote objective lens (O3) is oriented at 45 deg to re-image the tilted light sheet onto a camera. The ODO path simply images the light sheet from the illumination path directly onto a second camera. **(c-d)** An advantage of NODO is that the illumination and collection beams do not have to share one objective lens and can be oriented with a larger crossing angle, both of which enable superior axial and lateral resolution compared with NOSO, in which those parameters must trade off. (**e**) Furthermore, unlike ODO, which is extremely sensitive to refractive-index-mismatch at higher NAs (red curve), NODO uses a collection objective lens oriented in the normal (vertical) direction, which is much less sensitive to index-mismatch (green curve). The index-mismatch sensitivity for the low-resolution ODO collection path of the hybrid OTLS system is also shown (blue curve). Note that the index-mismatch is represented by the optical path difference, Δ*n* x *t*, where Δ*n* is the refractive-index difference between the holder material and immersion medium/tissue, and *t* is the thickness of the holder. A Strehl ratio of >0.8 is often considered ideal "diffraction-limited" imaging. **(f)** Finally, our hybrid OTLS system allows the user to trade-off between imaging speed and resolution as shown in the plot, roughly corresponding to the resolution levels that are achievable by a standard widefield microscope with a turret of 2X to 40X objective lenses (volumetric imaging speeds of ~ 0.3 mm^3 sec^{-1} to 3000 mm^3 sec^{-1}).

Supplementary Material

Supplementary Note 1 – NA- and FOV-limited imaging

Both collection objective lenses in the NODO and ODO paths provide more imaging information (i.e., space-bandwidth product) than current 2048 x 2048 pixel sCMOS cameras can capture. Therefore, the multi-scale capabilities of our system can be extended by changing the magnification (i.e., FOV) of both imaging paths on the sCMOS chip; either by zooming in until the imaging resolution is limited by the NA of the objective lens, or by zooming out until the tissue area that is imaged on the sCMOS camera chip is limited by the FOV of the objective lens. In the latter case, if the effective NA of the objective lens is not reduced, the resolution is determined by the pixel spacing (i.e. sampling ratio) on the sCMOS camera, according to the Nyquist criterion. However, in practice, imaging with a higher NA than necessary can introduce aberrations at the edges of the larger FOV. This is especially true for the ODO imaging path, where the SIMlens provides diminishing performance farther from the center of the FOV [16]. Therefore, for both the NODO and ODO paths, we reduce the effective NA to provide near-Nyquist sampling over the increased FOV. For the NODO path, this is achieved by switching O3 at the remote focus (**Supplementary Figure 6**), and for the ODO path this is achieved using a variable aperture near the back focal plane behind the collection objective lens (**Supplementary Figures 14 - 15**).

Supplementary Note 2 – Comparison to LSTM

Our hybrid system resembles the recently developed light-sheet theta microscopy system, with a key difference [11]. Instead of using a remote focus to re-image a tilted light sheet, LSTM scans both beams (with a complex and synchronized combination of lateral and axial scanning) to generate a virtual light sheet within the specimen that is orthogonal to the collection objective lens. To reject out-of-focus light, the scanning beams are synchronized to a confocal slit, which results in inefficient light collection (**Supplementary Figure 19**). This is in contrast to other light-sheet microscopy architectures (ODO, NODO, and NOSO) where the imaging plane is always co-planar with the light sheet.

Supplementary Note 3 – Multi-scale imaging with the NOSO architecture

With currently available commercial objective lenses (**Supplementary Figure 5**), multi-scale imaging at both mesoscopic and sub-micron resolution with a NOSO architecture is not possible. This is because no single objective lens currently provides sub-micron resolution over a mesoscopic FOV. Furthermore, it is not feasible to simply add a lower magnification imaging objective lens to an existing NOSO system (i.e., a NODO system, where the light sheet is still delivered through the primary objective lens and a second non-orthogonal imaging objective lens is used as a second imaging path). This is because the light sheet width would be constrained by the FOV of the primary objective lens and would not be able to take advantage of the larger FOV of the lower-magnification objective lens that is used to create the remote focus, O2. Therefore, multi-scale imaging with the NOSO architecture may only be possible in the future with the development of highly customized objective lenses (see **Supplementary Figure 20**). While these objective lenses would likely be prohibitively expensive to design and manufacture, the patent literature does contain recent examples of highly customized objective lenses designed specifically for whole slide scanners (e.g., US #8350904 which discloses a 0.90 NA objective lens with a 1.5 mm FOV and ~1 mm working distance [30]. However, this would require the relay lenses and both remote objective lenses to accommodate the same large FOV and high NA, which is not ideal for multi-scale imaging.

Supplementary Note 4 – Alternative NODO architecture

An alternative NODO configuration could use the CFI S Plan Fluor LWD 20XC and a customized O3 to maintain the full 0.483 NA of our O1. Several custom options for O3 include 20X water immersion objective lenses from Olympus and Zeiss, as well as the recently developed solid immersion AMS-AGY v1.0 objective lens from Special Optics. While the AMS-AGY v1.0 is the simplest option, the FOV of the objective lens is limited to 0.15 mm (diffraction-limited) and 0.25 mm (near diffraction-limited) which is too small for our design. On the other hand, using a water immersion objective lens requires sealing the water into a custom housing or prism with a cover glass. This is not compatible with the Olympus water objective lens, as it is not designed for use with a cover glass. Therefore, the only viable option is the Zeiss "W" Plan Apochromat 20X from. We developed a custom sleeve to house this objective lens, which seals water around the tip of the objective lens using a gasket and cover glass. When used for O3 and combined with a downstream zoom module (for example the Resolv4K, Navitar), this configuration provides the NA and FOV to simultaneously provide NA- and FOV-limited imaging. While we will continue to explore and test this configuration, these components add cost and complexity to the design. The physical layout, ZEMAX model, and the customized Zeiss water objective assembly are shown in **Supplementary Figure 13**.

System	**Hybrid OTLS**	**Ultramicroscope II (LaVision Biotec)**	**SmartSPIM (Lifecanvas)**	**Alpha3 (PhaseView)**	**ct-dSPIM (ASI)**	**CTLS (3I)**	**MuVi SPIM CS (Luxendo)**	**Lightsheet 7 (Zeiss)**
Illumination path	Single-sided	Double-sided	Double-sided	Double-sided	Single-sided	Double-sided	Double-sided	Double-sided
Collection path	Vertical (open-top)	Vertical	Vertical	Vertical	Vertical (inverted)	Vertical	Horizontal	Horizontal
Collection objective lenses	2X (NA = 0.10) 24X (NA = 0.70)	1.1X (NA = 0.10) 2X (NA = 0.50) 4X (NA = 0.35) 12X (NA = 0.53)	3.6X (NA = 0.20) 15X (NA = 0.40)	2X (NA = 0.14) 4X (NA = 0.28) 10X (NA = 0.50)	16X (NA = 0.40) 24X (NA = 0.70)	1X (NA = 0.20) 1.5X (NA = 0.37)	10X (NA = 0.50) 20X (NA = 1.00)	5X (NA = 0.16) 10X (NA = 0.50) 20X (NA = 1.00) 40X (NA = 1.00) 63X (NA = 1.00)
Horizontal FOV (mm)	11.0 (2X) 1.0 (24X)	22.6 (1.1X) 12.4 (2X) 6.2 (4X) 2.1 (12X)	3.7 (3.6X) 0.8 (15X)	11.0 (2X) 5.5 (4X) 2.2 (10X)	1.2 (16x) 1.0 (24x)	22.0 (1X) 14.7 (1.5X)	2.0 (10X) 1.0 (20X)	4.0 (5X) 2.0 (10X) 1.0 (20X) 0.5 (40X) 0.3 (63X)
Axial resolution (μm)	1.9 – 15.6	4.0 – 24.0	1.4 – 4.0	2.0 – 12.0	>1.0	3.0	2.0 – 8.0	2.0 – 14.0
Isotropic axial resolution?	No	No	No	No	No (single view) Yes (dual view)	No	No (single view) Yes (multi-view)	No
Refractive-index range	1.33 – 1.56	1.33 – 1.49 (1.1X) 1.50 – 1.57 (1.1X) 1.33 – 1.56 (2X) 1.33 – 1.41 (4X, 12X) 1.42 – 1.48 (4X, 12X) 1.49 – 1.57 (4X, 12X)	1.33 – 1.56	1.33 – 1.56	1.33 – 1.56	1.33 – 1.56	1.33 – 1.51 (10X) 1.44 – 1.50 (20X)	1.33 – 1.58 (5X) 1.33 (10X) 1.33, 1.38, 1.45, 1.53 (20X) 1.33 (40X) 1.33 (63X)
Maximum imaging deoth (mm)	10	16 – 17 (1.1X) 10 (2X) 15 – 16 (4X) 8.5 – 10.9 (12X)	12	15	5 (16X) 2 (24X)	25	12	10
Maximum specimen lateral size (X x Y, mm)	Unconstrained	10 x 10	20 x 25 (standard) 30 x 55 (extended)	15 x 15 (standard) 15 x 25 (extended)	Unconstrained	25 x 25	12 x 19	10 x 50

Supplementary Table 1 | Commercially available cleared-tissue light-sheet microscopes. The specifications of commercial light-sheet microscopes in comparison to our new hybrid OTLS system. For the collection path, “open-top” denotes that the objective lenses are below the specimen and enable unconstrained lateral imaging, whereas “inverted” denotes that the objective lenses are above the specimen, where unconstrained lateral imaging is also possible. Many of these specifications were obtained from a recent mesoSPIM publication [13].

System	**Hybrid OTLS**	**mesoSPIM V5**	**ctASLM**	**LSTM**	**COLM**
Illumination path	Single-sided	Double-sided	Single-sided	Double-sided	Dual-sided
Collection path	Vertical (open-top)	Horizontal	Horizontal	Vertical (inverted)	Vertical
Collection objective lenses	2X (NA = 0.10) 24X (NA = 0.70)	1X (NA = 0.25)	16X (NA = 0.40) 24X (NA = 0.70)	10X (NA = 0.60) 25X (NA = 1.00)	10x (NA = 0.60) 25x (NA = 1.00)
Horizontal FOV (mm)	11.0 (2X) 1.0 (24X)	20.0	1.0 (16X) 1.2 (24X)	2.0 (10X) 0.8 (25X)	2.0 (10X) 0.8 (25X)
Axial resolution (μm)	1.9 – 15.6	6.5	0.3 – 0.6	4.0 – 11.0	1.2
Isotropic axial resolution?	No	Yes (ASLM)	Yes (ASLM)	No	No
Refractive-index range	1.33 – 1.56	1.33 – 1.56	1.33 – 1.56	1.33 – 1.52 (10X) 1.41 – 1.52 (25X)	1.33 – 1.52 (10X) 1.41 – 1.52 (25X)
Maximum imaging depth (mm)	10	52	12 (16x) 10 (24x)	8	8
Maximum specimen lateral size (X x Y, mm)	Unconstrained	52 x 100	12 x 12 (16x) 10 x 10 (24x)	Unconstrained	45 x 45

Supplementary Table 2 | Academic cleared-tissue light-sheet microscopes. The specifications of academic light-sheet microscopes in comparison to our new hybrid OTLS system [11-14]. For the collection path, “open-top” denotes that the objective lenses are below the specimen and enable unconstrained lateral imaging, whereas “inverted” denotes that the objective lenses are above the specimen, where unconstrained lateral imaging is also possible.

	ODO imaging path					**NODO imaging path**									
	n = 1.33														
Collection NA	0.03	0.05	0.08	0.11	0.13	0.36	0.39	0.41	0.44	0.47	0.49	0.52	0.55	0.57	0.60
Illumination NA	0.02	0.02	0.03	0.03	0.04	0.06	0.06	0.07	0.07	0.07	0.07	0.07	0.08	0.08	0.08
Lateral resolution (µm)	9.46	4.73	3.15	2.36	1.89	0.70	0.65	0.61	0.57	0.54	0.51	0.48	0.46	0.44	0.42
Axial resolution (µm)	15.61	11.03	9.00	7.78	6.94	3.82	3.61	3.40	3.21	3.03	2.86	2.70	2.54	2.40	2.26
	n = 1.46														
Collection NA	0.03	0.06	0.09	0.12	0.15	0.39	0.42	0.45	0.48	0.51	0.54	0.57	0.60	0.63	0.66
Illumination NA	0.02	0.03	0.03	0.04	0.04	0.07	0.07	0.07	0.08	0.08	0.08	0.08	0.08	0.09	0.09
Lateral resolution (µm)	8.62	4.31	2.87	2.15	1.72	0.64	0.59	0.56	0.52	0.49	0.47	0.44	0.42	0.40	0.38
Axial resolution (µm)	14.22	10.05	8.20	7.09	6.32	3.48	3.28	3.10	2.92	2.76	2.60	2.46	2.32	2.19	2.06
	n = 1.56														
Collection NA	0.03	0.06	0.09	0.12	0.16	0.42	0.45	0.48	0.51	0.55	0.58	0.61	0.64	0.67	0.70
Illumination NA	0.02	0.03	0.03	0.04	0.04	0.07	0.08	0.08	0.08	0.08	0.09	0.09	0.09	0.09	0.09
Lateral resolution (µm)	8.06	4.03	2.69	2.02	1.61	0.60	0.56	0.52	0.49	0.46	0.44	0.41	0.39	0.38	0.36
Axial resolution (µm)	13.31	9.41	7.67	6.63	5.91	3.26	3.07	2.90	2.74	2.58	2.44	2.30	2.17	2.05	1.93

Supplementary Table 3 | Imaging specifications. Various combinations of imaging specifications (lateral and axial resolution) that can be achieved with the hybrid OTLS system as a function of collection and illumination NA. Specified for a refractive-index, *n*, of 1.33, 1.46, and 1.56.

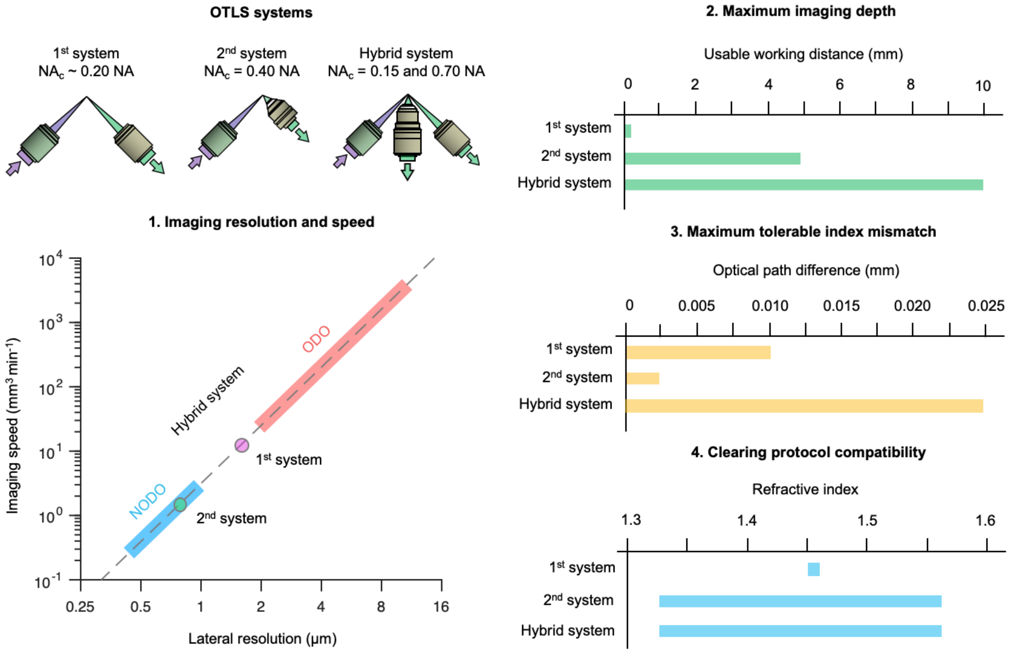

Supplementary Figure 1 | Comparison of new and past OTLS configurations. The specifications (imaging resolution, speed, imaging depth, index-mismatch sensitivity, and clearing-protocol compatibility) of our new hybrid OTLS system, compared to two previous generations of OTLS microscopes (fixed-resolution systems) [15, 17].

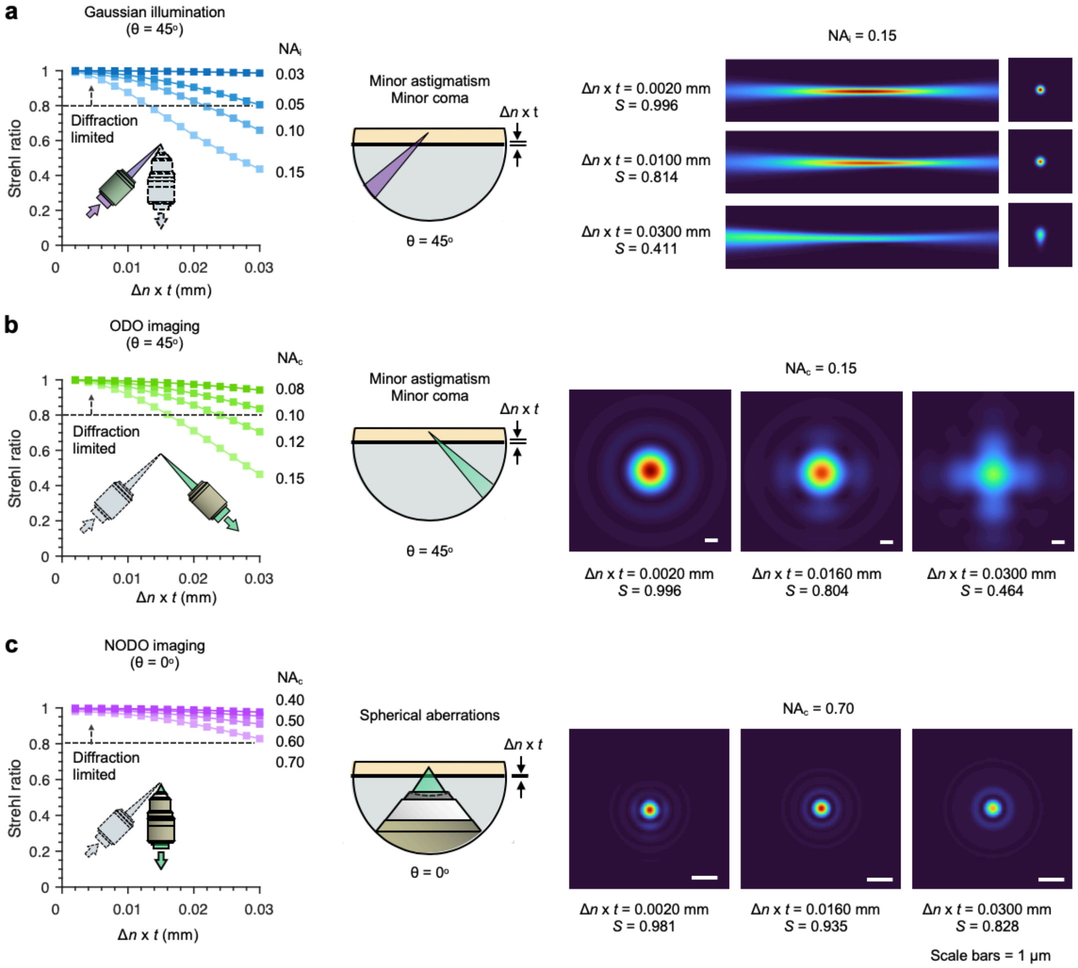

Supplementary Figure 2 | Index-mismatch sensitivity of hybrid OTLS system. ZEMAX simulations of the index-mismatch sensitivity for all three optical paths in the hybrid OTLS system. The index-mismatch is given by the optical path difference, Δ*n* x *t*, where Δ*n* is the refractive-index difference between the holder and immersion medium/tissue, and *t* is the thickness of the holder. **(a)** Results for a Gaussian illumination light sheet with corresponding intensity cross-sections. The angle of illumination is 45 deg **(b)** Results for the ODO collection path, with corresponding point spread functions. The angle of collection is also 45 deg **(c)** Results for the NODO collection path, with corresponding point spread functions. The angle of collection is 0 deg. In **(a-c)**, NA$_i$ refers to illumination NA, and NA$_c$ refers to collection NA. Note that a Strehl ratio of >0.8 is often considered ideal (“diffraction-limited” imaging).

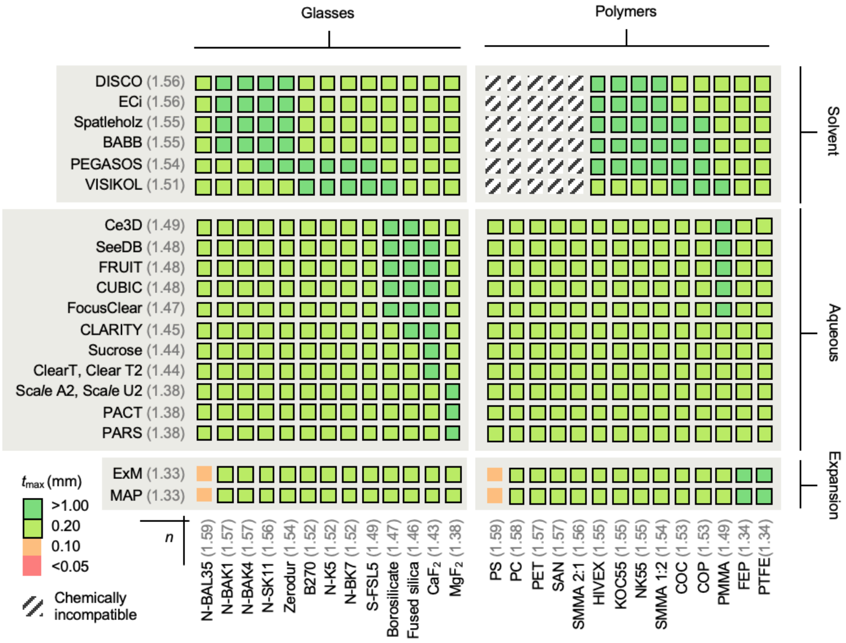

Supplementary Figure 3 | Compatible combinations of clearing protocols and holder materials. Based on the ZEMAX index-mismatch simulations, a clearing protocol and holder material compatibility matrix can be generated. Based on the maximum index-mismatch, the corresponding maximum specimen holder thickness, t_{max} is calculated. Thickness values greater than 0.20 mm are considered to be practically feasible. The hybrid OTLS system is largely insensitive to index-mismatch, enabling the combination of virtually any clearing protocol and specimen-holder material.

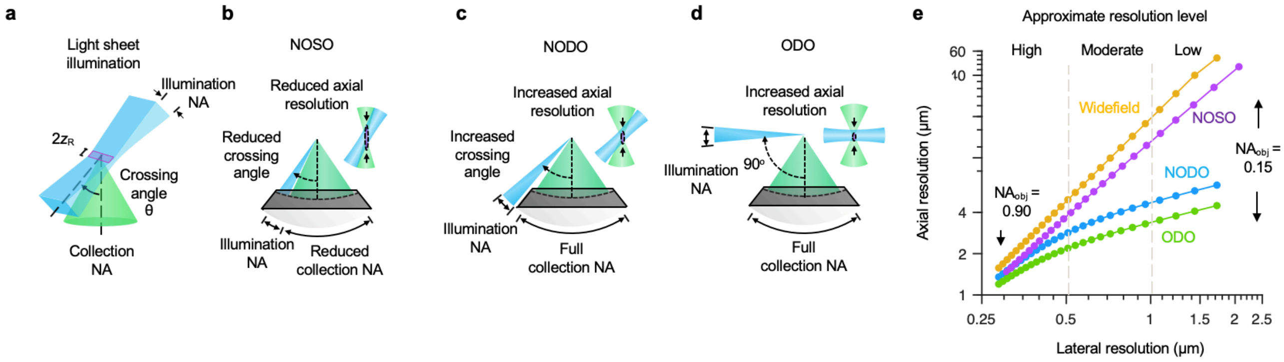

Illumination NA	NOSO	NODO	ODO	Simulation inputs
FOV = 2048 x 0.61 x λ / (NA_{obj}) / 2	θ = $\sin^{-1}(NA_{obj} / n) - \sin^{-1}(NA_i / n)$	θ = 45 deg.	θ = 90 deg.	λ = 0.5 µm
$2z_R$ = FOV / 8	$NA_c = NA_{obj} - NA_i / 2$	$NA_c = NA_{obj}$	$NA_c = NA_{obj}$	n = 1.5
$NA_i = z_R \times \lambda / \pi / n$				NA_{obj} = 0.15 – 0.9 (0.03 steps)

Supplementary Figure 4 | Extended comparison of NOSO, NODO, and ODO optical performance. (a) For a given objective lens NA, the FOV at Nyquist sampling was calculated for a 2048 x 2048 pixel sCMOS camera. The illumination NA was then chosen such that the Rayleigh length, $2z_R$, would fill 1/8 of the chip (256 pixels). This is a reasonable vertical height for systems that perform stage-scanned imaging, such as the current hybrid OTLS system. **(b)** For the NOSO architecture, there is a coupled relationship between the illumination NA, collection NA, and crossing angle of the two beams. **(c)** For the NODO architecture, the paths are decoupled. **(d)** For the ODO architecture, the paths are decoupled and orthogonal to one another. **(e)** Simulation results for the lateral and axial resolution of the NOSO and NODO architectures for objective lens NA's (NA_{obj}) ranging from 0.15 – 0.90. At low and moderate objective lens NAs, there is a substantial performance benefit of NODO vs. NOSO, approaching that of ODO (but with superior imaging depth and tolerance to index-mismatch). The optical performance for widefield microscopy is also shown.

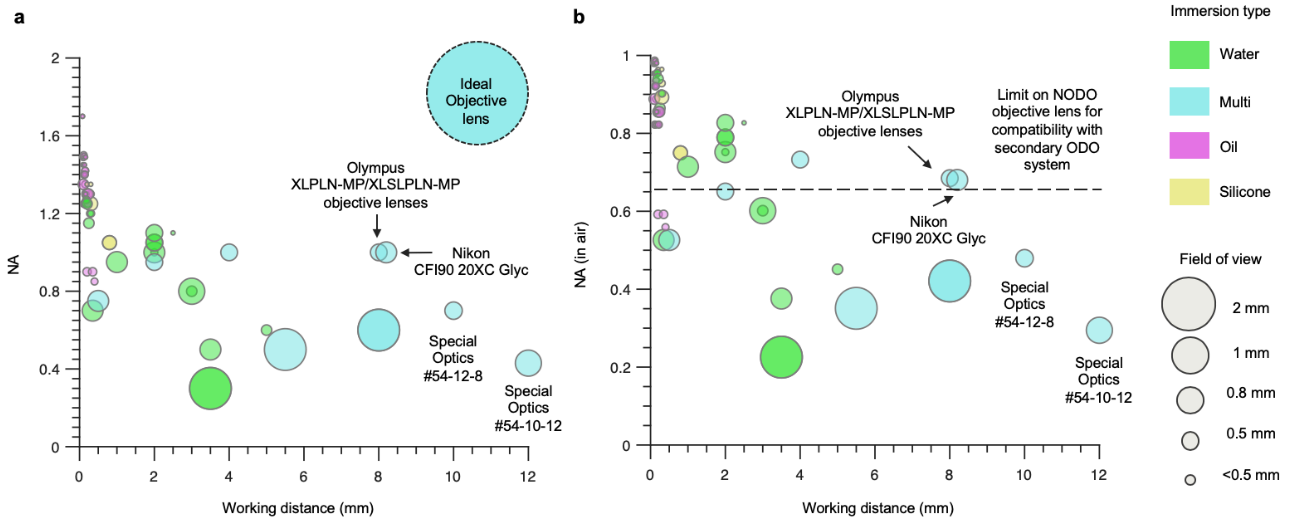

Supplementary Figure 5 | Candidate objective lenses for NODO imaging. (a) Plot summarizing objective lenses currently available from Olympus, Nikon, and Special Optics for NODO imaging of cleared tissues. The color of each data point denotes the immersion type (water, multi, oil, or silicone) and the size of the point denotes the field of view. As can be seen, in current objective lenses, there is a distinct trade-off between magnification, NA, and working distance. An ideal objective lens, with a large field of view, high NA, and long working distance is also plotted. The multi-immersion objective lens (Special Optics #54-12-8) used in the current system's NODO imaging path is also highlighted. **(b)** The same data plotted with the y-axis showing the NA in air as opposed to the immersion medium. In this plot, a line is drawn above which hybrid imaging would no longer be possible, as the optical cone angle of the NODO imaging objective lens would surpass 45 deg (NA > 0.65 in air), thereby preventing additional optical paths at 45 deg for ODO imaging. For example, the Olympus XLPLN/XLSPLN and Nikon CFI90 20XC Glyc objective lenses would be attractive for NODO imaging but would not allow for multi-scale imaging with a separate ODO imaging path due to its large NA. Note, the level of chromatic aberration correction for each lens is not indicated in either plot. A data file containing the information used to generate the plots as available as **Supplementary Data**.

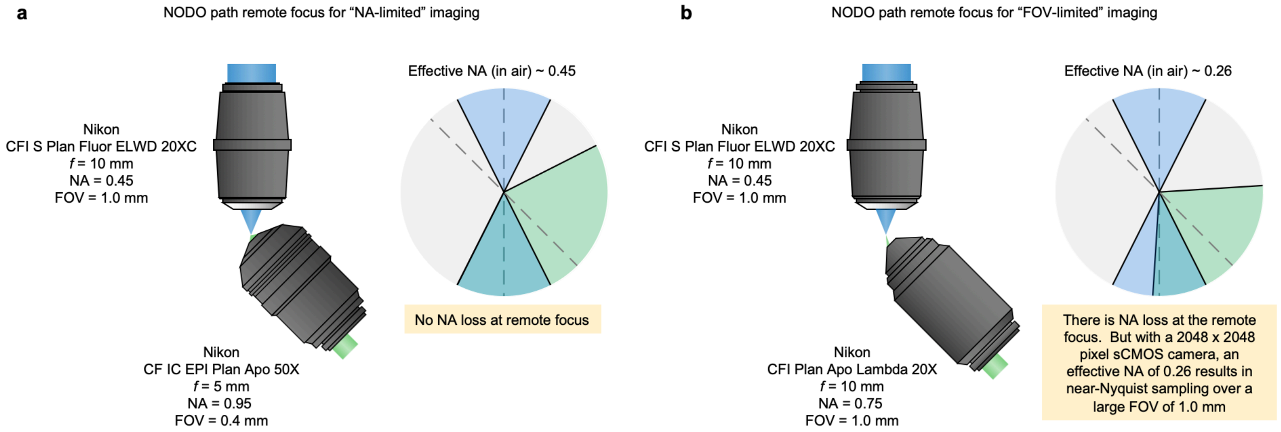

Supplementary Figure 6 | Remote-focus layout for NODO imaging. Our NODO imaging architecture enables the use of commercial air objective lenses at the remote focus, as opposed to bespoke objective assemblies **(a)** Using a crossing angle of 45 deg, the effective NA of the NODO imaging path is a lossless ~0.45 (in air) when using a 50x 0.95 NA air objective lens. This configuration provides NA-limited imaging **(b)** By switching to a 20x 0.75 NA remote objective lens, the effective NA is reduced to ~0.26 (in air). Despite the loss in effective NA, Nyquist sampling at this NA on a standard 2048 x 2048 pixel sCMOS camera yields a field of view of ~ 1.0 mm. Therefore, this configuration provides FOV-limited imaging.

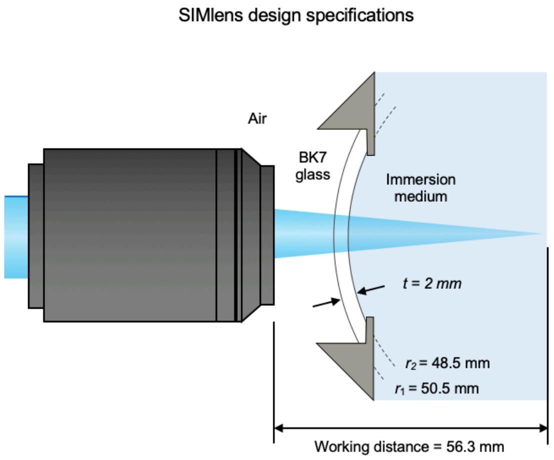

SIMlens design specifications

Supplementary Figure 7 | SIMlens specifications. The specifications of the SIMlens used on the illumination and ODO optical paths are shown. The lens is fabricated of BK7 glass and is 2-mm thick. The radii of curvature of the lens surfaces are 48.5 and 50.5 mm respectively (identical center of curvature). The lens is positioned such that the center of curvature for both lens surfaces is coincident with the on-axis focus of the objective lens. This causes all rays traveling to or from this focal point to transition between the SIMlens interfaces at a normal (90-deg) angle where refraction is negligible, thereby suppressing any aberrations.

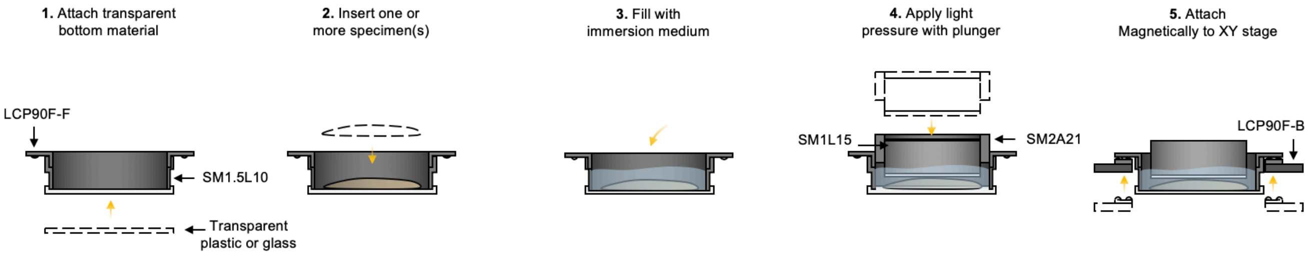

Supplementary Figure 8 | Specimen mounting for hybrid OTLS system. Our new hybrid OTLS system using an improved specimen holder and mounting procedure. The circular holder features a bottom thread, to which an interchangeable transparent bottom material can be attached. Specimens are then inserted into the holder from the top, and the holder is filled with an index-matching immersion medium. Light pressure is then applied to the top of the tissue using a plunger. The bottom surface of the plunger is the same transparent material as the bottom of the holder, which reduces back reflections when imaging the deepest surface of the specimen. Finally, the entire specimen holder is magnetically attached to the XY stage.

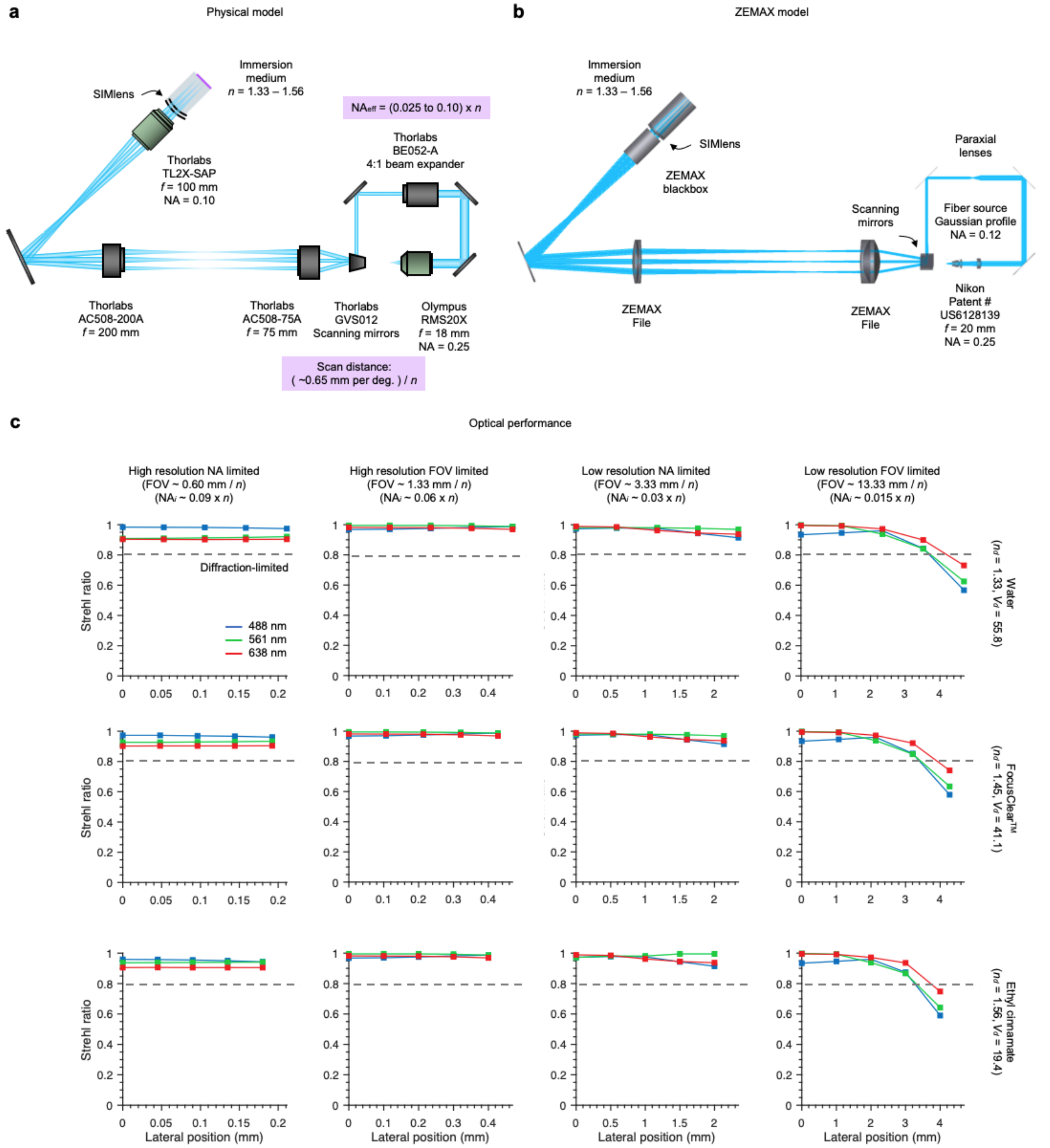

Supplementary Figure 9 | Illumination optics models. (a) The physical model of the hybrid OTLS system illumination optics is shown. Light is collimated using a 20X objective lens and passed through a 4:1 variable beam expander. The adjusted beam is then scanned using a pair of galvanometric scanning mirrors, which is then relayed to the back focal plane of the 2X illumination objective lens using a pair of relay lenses. Finally, the light passes through the SIMlens and into the specimen. The effective illumination NA can be varied from ~ 0.025 – 0.10, multiplied by the refractive-index of the immersion medium, *n*. The width of the light sheet can similarly be tuned using one of the scanning mirrors, which provides a scanning distance of ~0.65 mm / deg, divided *n*. The second scanning mirror is used to align the light sheet to the focal planes of the collection objective lenses **(b)** Corresponding ZEMAX model. Lens prescriptions or blackbox files were available for all components, except for the beam expander and collimation objective lens. The beam expander was modeled using a pair of paraxial lenses, and the collimation objective was modeled using US Patent #6128139. **(c)** Results for the Strehl ratio as a function of lateral position across the width of the sheet. The four columns correspond to the four imaging modes, high-resolution (NODO) NA-limited and FOV-limited, and low-resolution (ODO) NA-limited and FOV-limited. The three rows correspond to different immersion media, water (n ~ 1.33), FocusClear^{TM} (n ~ 1.46), and ethyl cinnamate (n ~ 1.56). The colored lines on each plot denote wavelength, 488 nm (blue), 561 nm (green), and 638 nm (red).

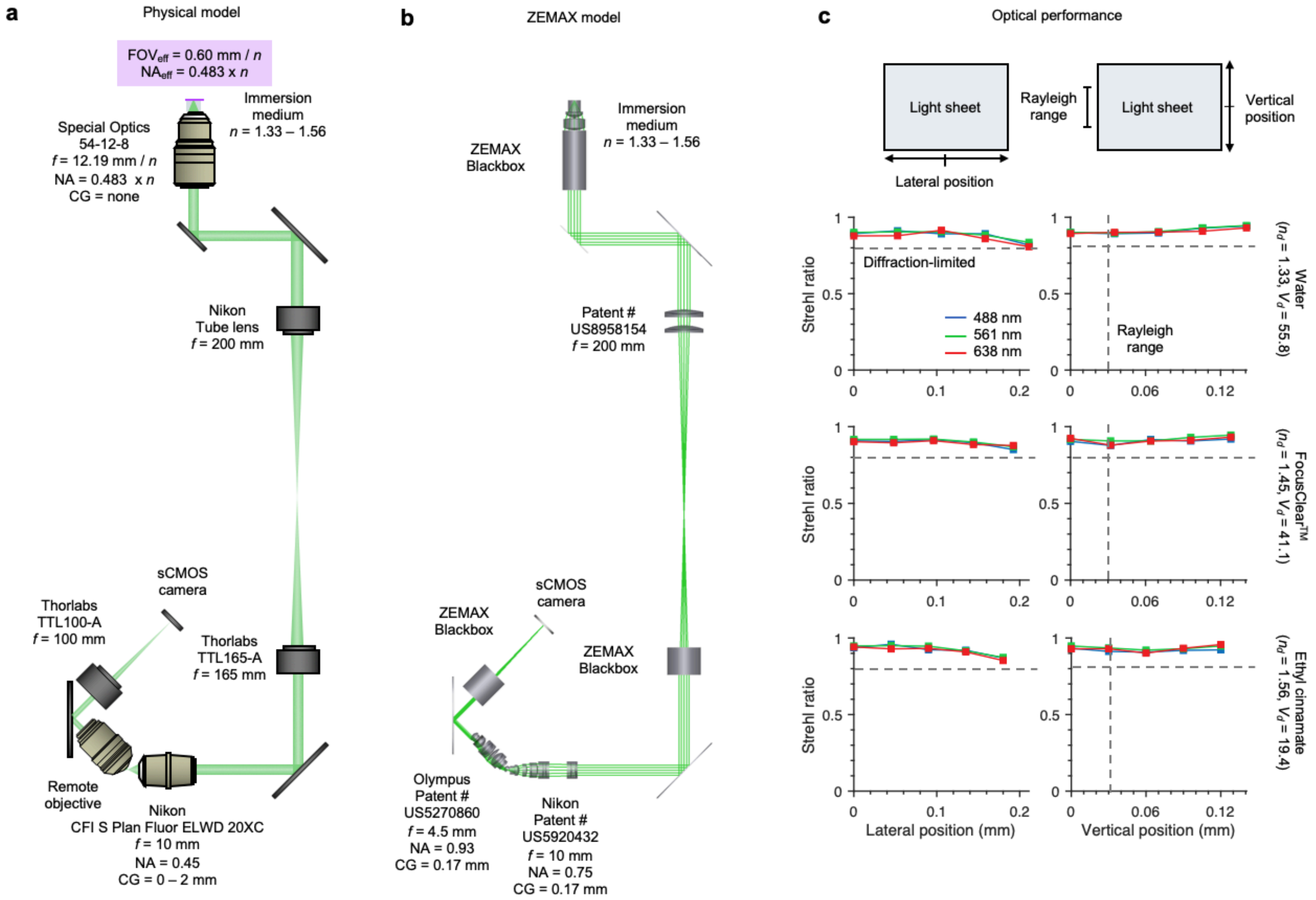

d

Remote objective options for NA-limited NODO imaging

Company	Model #	Cover glass	NA	FOV	NA$_{eff}$	M$_{total}$	Nyquist rate
Nikon	CFI Plan Apo Lambda 40XC	0.11 – 0.23 mm	0.95	0.5 mm	0.45 x *n*	20.00 x *n*	2.17
Nikon	CF IC EPI Plan Apo 50X	None	0.95	0.4 mm	0.45 x *n*	25.00 x *n*	2.71
Olympus	UPLSAPO40X2	0.11 – 0.23 mm	0.95	0.5 mm	0.45 x *n*	22.22 x *n*	2.41
Olympus	MPLAPON50X	None	0.95	0.4 mm	0.45 x *n*	27.78 x *n*	3.01

Supplementary Figure 10 | NA-limited NODO collection optics model. (a) The physical model of the NA-limited NODO collection optics within the hybrid OTLS system. Fluorescence is collected by a multi-immersion objective lens (*f* = 12.19 / *n*) and relayed to a remote focus using tube lenses (*f* = 200 and 165 mm), and a 20X objective lens (*f* = 10 mm). For aberration free imaging, the total magnification from the specimen to the remote focus should be equal to *n*. For the optics chosen, the total magnification is extremely close: ~0.994 *n*. The remote imaging arm is tilted by 45 deg and uses a remote objective lens and tube lens (*f* = 100 mm) to image the remote focus onto a sCMOS camera. The effective numerical aperture of the multi-immersion objectivelens is 0.45 x *n*, with an effective FOV of 0.60 mm / *n*. **(b)** Corresponding ZEMAX model. Lens prescriptions or blackbox files were available for all components, except for the remote imaging objective lenses. For these objective lenses, US Patent # 5920432 and #5270860 were used. **(c)** Results for the Strehl ratio as a function of lateral position across the width of the sheet (left) and along the length of the sheet (right). The three rows correspond to different immersion media, water (*n* ~ 1.33), FocusClear™ (*n* ~ 1.46), and ethyl cinnamate (*n* ~ 1.56). The colored lines on each plot denote wavelength, 488 nm (blue), 561 nm (green), and 638 nm (red). **(d)** Various options for the remote objective lens, and the corresponding imaging specifications.

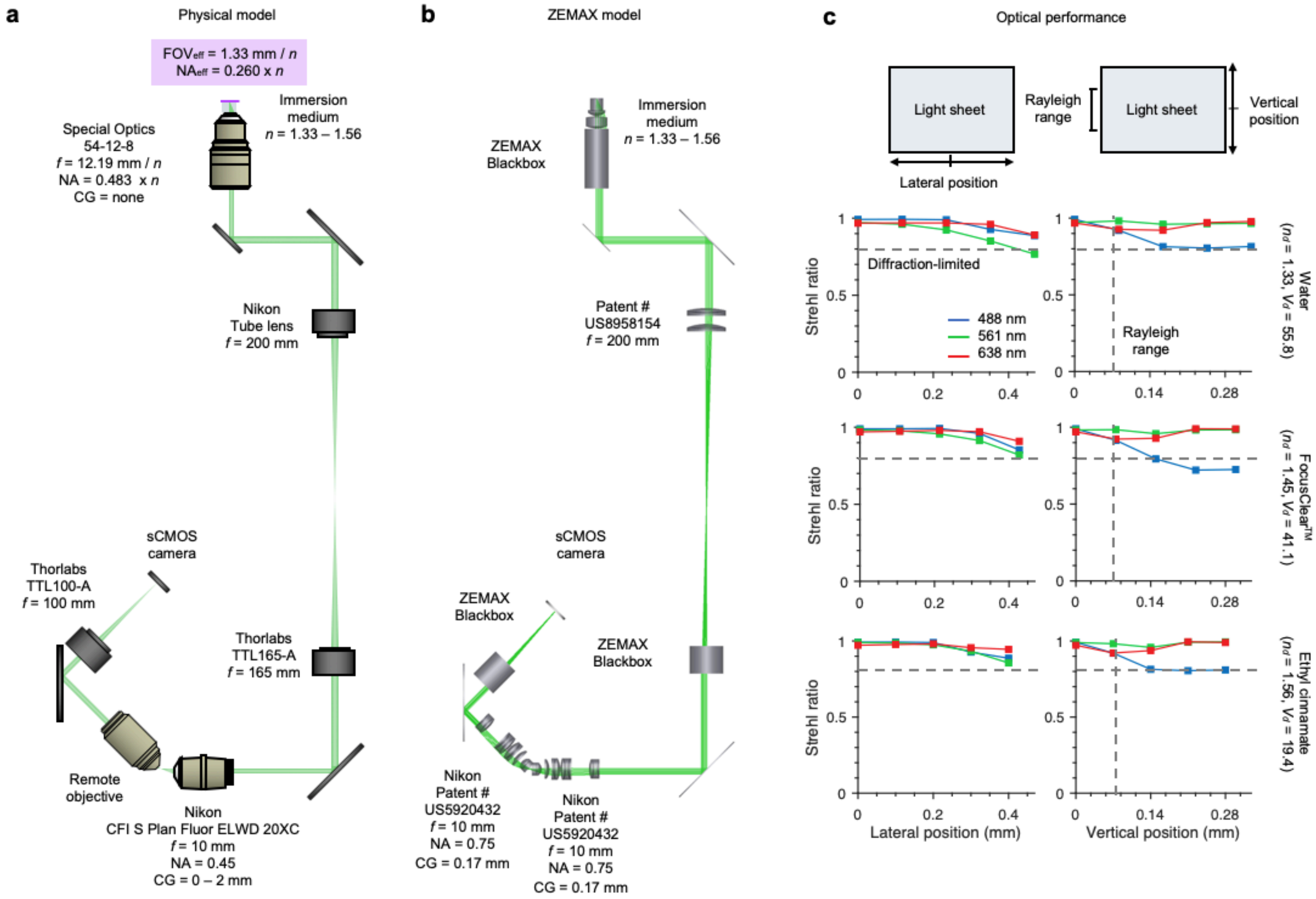

d

Remote objective options for FOV-limited NODO imaging

Company	Model #	Cover glass	NA	FOV	NA_{eff}	M_{total}	Nyquist rate
Nikon	CFI Plan Apo Lambda 20X	0.17 mm	0.75	1 mm	~0.26 x *n*	10.00 x *n*	2.02
Nikon	CFI Super Fluor 20X	0.17 mm	0.75	1 mm	~0.26 x *n*	10.00 x *n*	2.02
Nikon	CFI S Plan Fluor LWD 20XC	0 – 1.8 mm	0.70	1 mm	~0.22 x *n*	10.00 x *n*	2.39
Olympus	UPLSAPO20X	0.17 mm	0.75	1 mm	~0.26 x *n*	11.11 x *n*	2.24
Olympus	UPLXAPO20X	0.17 mm	0.80	1 mm	~0.29 x *n*	11.11 x *n*	2.01
Olympus	UCPLFLN20X	0 – 1.6 mm	0.70	1 mm	~0.22 x *n*	11.11 x *n*	2.65

Supplementary Figure 11 | FOV-limited NODO collection optics model. (a) The physical model of the FOV-limited NODO collection optics in the hybrid OTLS system. The optics are identical to Supplementary Figure 7, except the imaging arm now uses a 20X remote air objective lens and the same tube lens (*f* = 100 mm) to image the remote focus onto a sCMOS camera. **(b)** Corresponding ZEMAX model. Lens prescriptions or blackbox files were available for all components, except for the remote imaging objective lenses. For both objectives lenses, US Patent # 5920432 was used. **(c)** Results for the Strehl ratio as a function of lateral position across the width of the sheet (left) and along the length of the sheet (right). **(d)** Various options for the remote objective lens, and the corresponding imaging specifications.

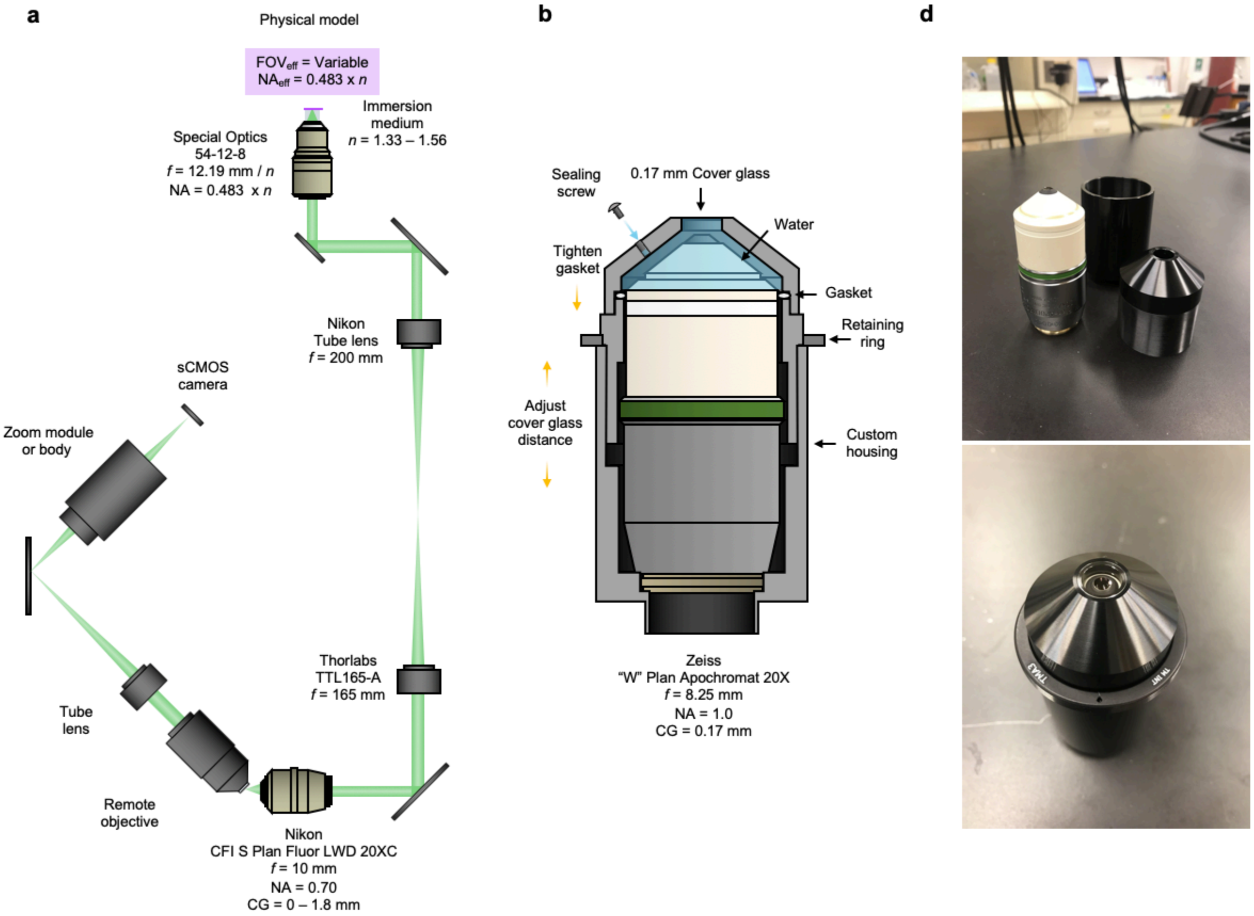

d

Remote objective options for NA-limited NODO imaging

Company	Model #	Cover glass	NA	FOV	NA$_{eff}$	M$_{total}$	Nyquist rate
Zeiss	"W" Plan Apochromat 20X	0.17 mm	1.0	1 mm	0.483 x n	Variable	Variable
Olympus	XLUMPLFLN20XW	None	1.0	1 mm	0.483 x n	Variable	Variable
Special Optics	AMS-AGY v1.0 (40X)	None	1.0	0.15 – 0.25 mm	0.483 x n	Variable	Variable

Supplementary Figure 12 | Alternative NODO collection optics model. (a) The physical model of alternative NODO collection optics is shown. Fluorescence is collected by a multi-immersion objective lens (f = 12.19 / n) and relayed to a remote focus using tube lenses (f = 200 and 165 mm), and a 20X objective lens (f = 10 mm). The remote imaging arm is tilted by 45 deg and uses a remote objective lens and tube lens (f = 100 mm) to image the remote focus onto a sCMOS camera. By using a liquid or solid immersion remote objective lens, the full NA is maintained, and the effective NA of the system is 0.483 x n **(b)** Custom designed sleeve to convert a Zeiss "W" Plan Apochromat 20X objective lens into a remote objective assembly. **(c)** Results for the fabricated sleeve shown in **(b)**. **(d)** Various options for the remote objective lens, and the corresponding imaging specifications.

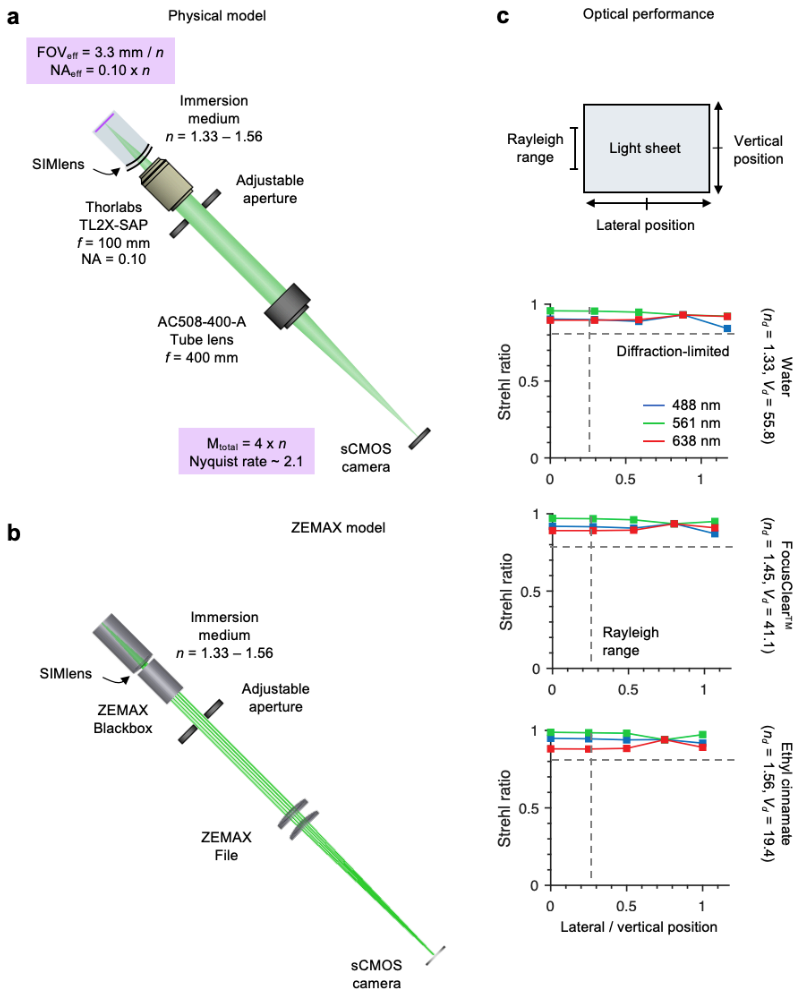

Supplementary Figure 13 | NA-limited ODO collection optics model. (a) The physical model of the NA-limited ODO collection optics within a hybrid OTLS system. Fluorescence is collected by a 2X (NA = 0.10) air objective lens. The objective lens is combined with the SIMlens, which provides multi-immersion compatibility, and increases the numerical aperture of the objective lens by *n*. Light is focused onto the sCMOS camera using a long focal length tube lens (*f* = 400 mm). The effective numerical aperture of the SIMlens and air objective lens is 0.10 x *n*, with an effective FOV of 3.33 mm / *n*. The total magnification of the imaging arm is 4 x *n*, which yields a Nyquist sampling rate of ~ 2.1 on the sCMOS camera. **(b)** Corresponding ZEMAX model. Lens prescriptions or blackbox files were available for all components. **(c)** Results for the Strehl ratio as a function of lateral position across the width of the sheet or along the length of the sheet. Unlike Supplementary Figures 7-8, where the two directions are modeled independently due to the tilted remote focus, the two directions are identical and symmetric for the ODO imaging path.

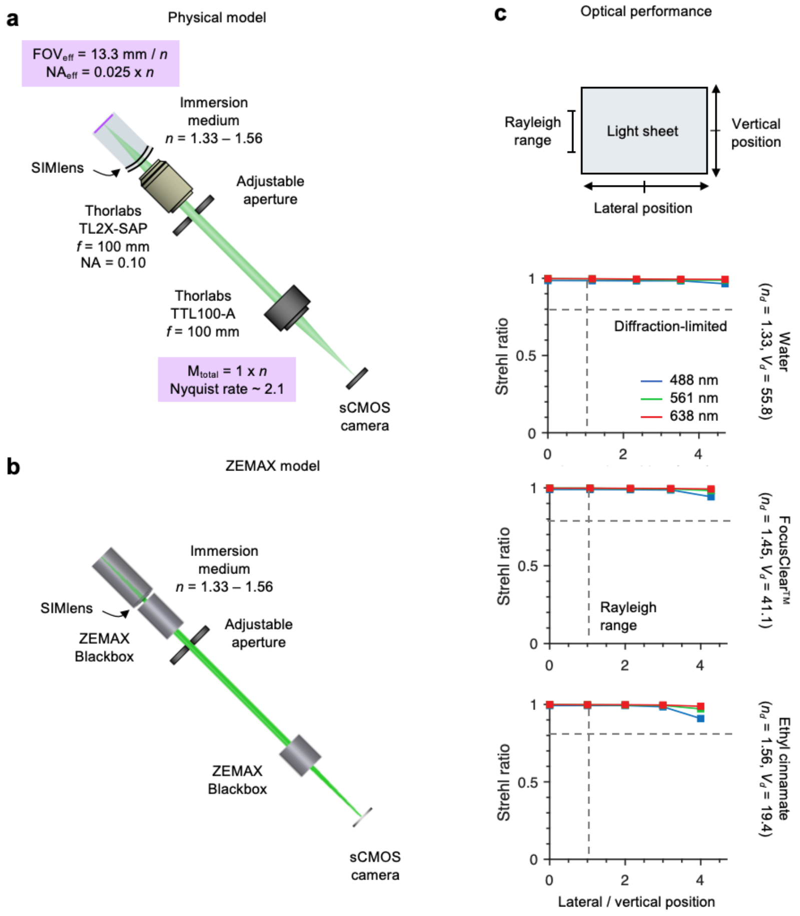

Supplementary Figure 14 | FOV-limited ODO collection optics model. (a) The physical model of the FOV-limited ODO collection optics in the hybrid OTLS system. Fluorescence is collected by a 2X (NA = 0.10) air objective lens. The objective lens is combined with a SIMlens, which provides multi-immersion compatibility, and increases the numerical aperture of the objective lens by *n*. Light is focused onto the sCMOS camera using a long focal length tube lens (*f* = 100 mm). The effective numerical aperture of the SIMlens and air objective lens is 0.025 x *n*, with an effective FOV of 13.33 mm / *n*. The total magnification of the imaging arm is 1 x *n*, which yields a Nyquist sampling rate of ~ 2.1 on the sCMOS camera. **(b)** Corresponding ZEMAX model. Lens prescriptions or blackbox files were available for all components. **(c)** Results for the Strehl ratio as a function of lateral position across the width of the sheet or along the length of the sheet. Unlike Supplementary Figures 7-8, where the two directions are modeled independently due to the tilted remote focus, the two directions are identical and symmetric for the ODO imaging path.

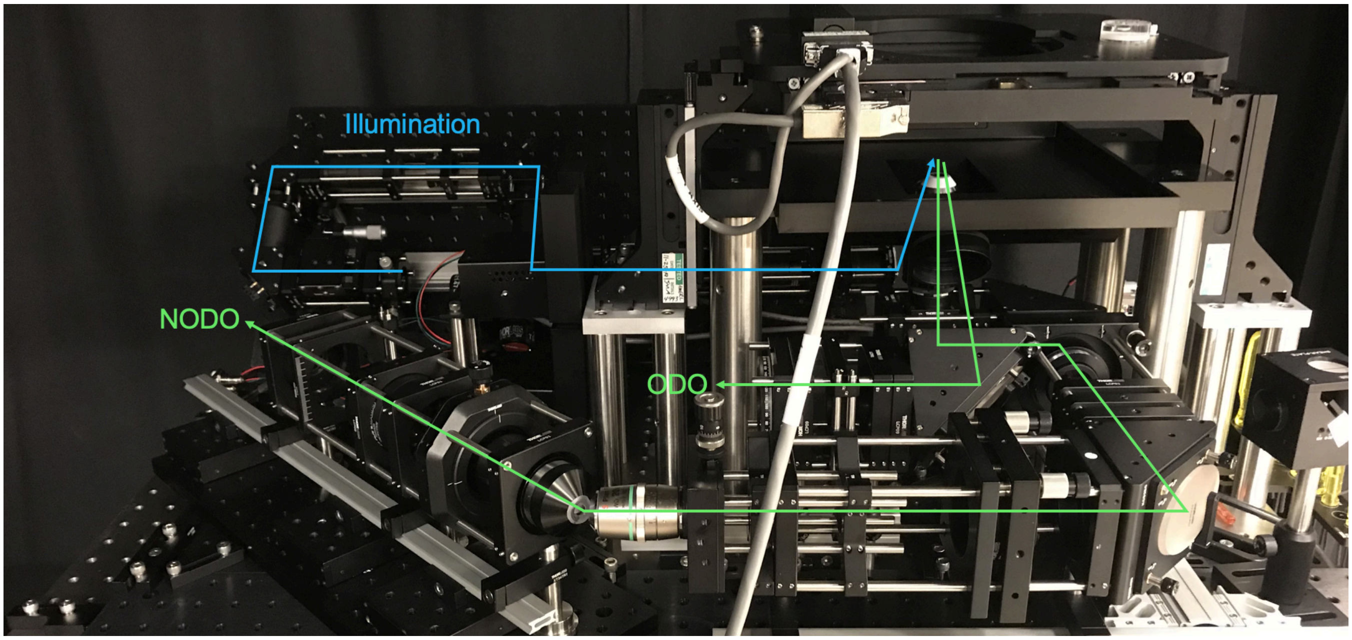

Supplementary Figure 15 | Hybrid OTLS system in practice. (a) Photograph of the hybrid OTLS system. The illumination optics (blue line) are housed on a single 18 x 36 in. breadboard angled at 45 deg. The NODO and ODO optics (green lines) are placed on flat breadboards. The NODO imaging optics are housed on a series of connected breadboards, which can be translated in one direction to adjust the distance between the imaging optics and the back focal plane (BFP) of the multi-immersion objective lens. This enables fine alignment when switching the immersion medium, as the axial position of the BFP of the objective lens is a function of refractive-index, n. The position of the BFP relative to the flange of the objective lens is approximately -11.75 mm - 22.90 mm x n + 5.87 mm x n^2. Finally, the remote objective lens, final tube lens, and sCMOS camera are all positioned atop another breadboard, which can be translated and rotated to align the remote imaging arm with respect to the remote focus.

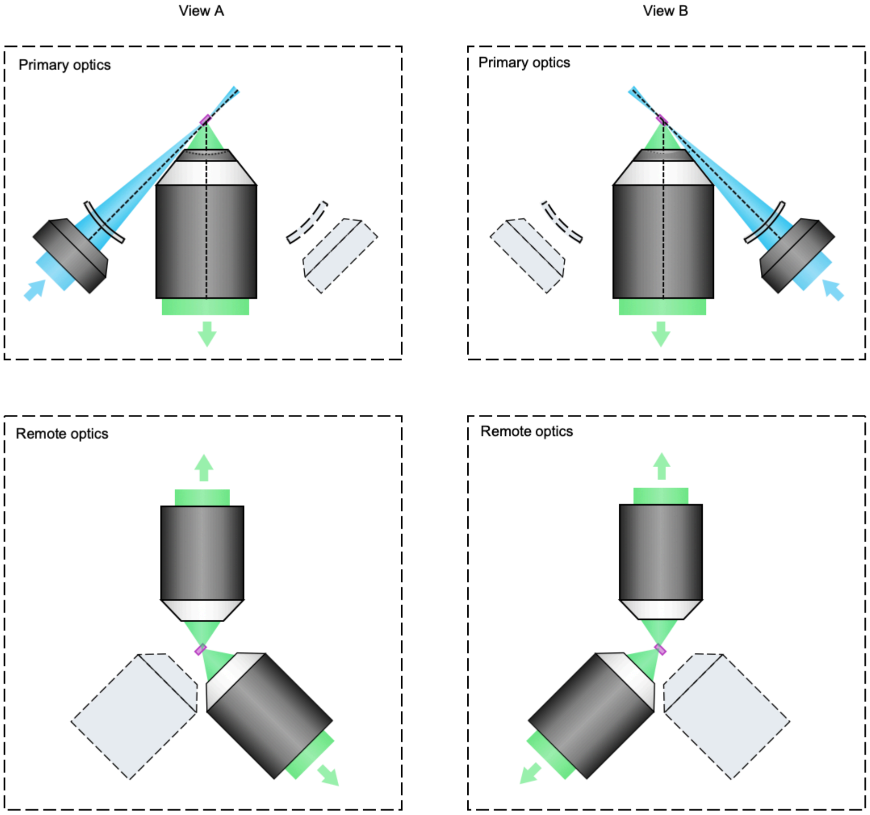

Supplementary Figure 16 | Dual-view hybrid OTLS system. Although in the current hybrid system, only one of the angled optical paths is used for illumination, and the other for ODO imaging, in the future both paths could be used for illumination and collection. As shown, this would yield two views (A and B) of the specimen, which could be input into a fusion deconvolution algorithm to achieve more isotropic resolution for both NODO imaging path. It is important to note that it would be challenging to accommodate two remote objective lenses for NOSO designs due to the increased tilt angle at the remote focus, which often necessitates bespoke objective lenses with unique geometric constraints. However, our NODO design reduces the required tilt angle, and therefore may permit the use of two angled air objective lenses (off-the-shelf) at the remote focus.

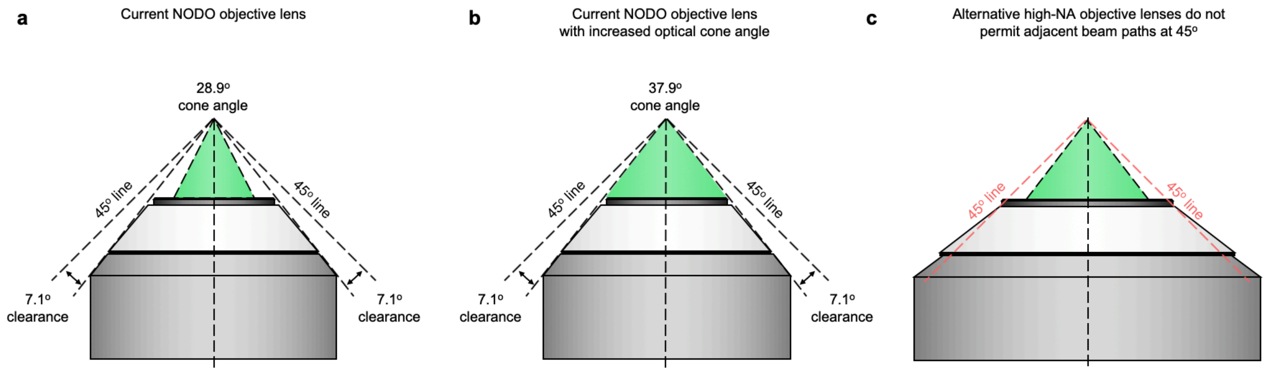

Supplementary Figure 17 | Considerations for NODO objective lens. (a) Schematic of the current NODO objective lens. The mechanical housing of the objective lens permits optical paths at 45 deg on both sides, with a maximum cone angle of 7.1 deg (NA ~ 0.12 in air). **(b)** The current NODO objective lens leaves ~ 9 deg between the optical and mechanical cone angles. Theoretically, the optical cone angle could be expanded from 28.9 to 37.9 deg in a future customized multi-immersion objective lens. In practice, this angle would be slightly less when accounting for the objective lens' finite FOV. **(c)** The majority of alternative high-NA immersion objective lenses (e.g., NA ~ 1.0) have mechanical housings that do not permit optical paths at 45 deg for the addition of ODO imaging.

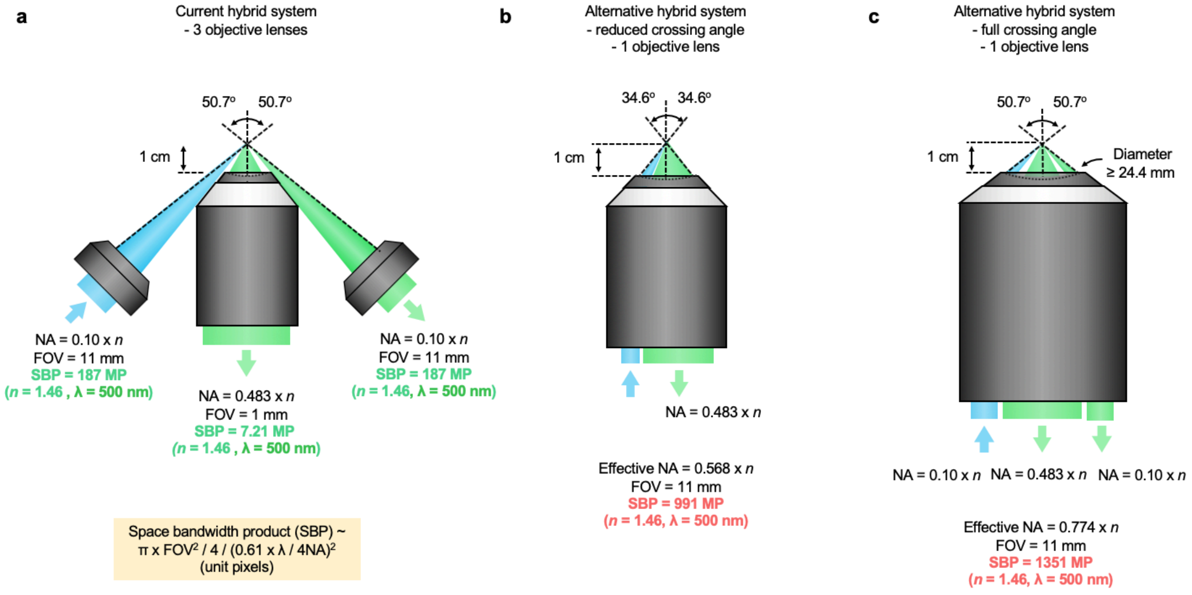

Supplementary Figure 18 | Alternative designs based on customized objective lenses. (a) The current hybrid OTLS system uses three objective lenses for illumination, high-resolution NODO imaging, and low-resolution ODO imaging. These objective lenses are all commercially available. **(b)** In theory, all three optical paths could be incorporated into a single objective lens. This theoretical objective lens would require an effective NA of 0.568 (in air) and a large 11 mm field of view (FOV). This NA would reduce the crossing angle of the illumination and collection beam paths but provide identical NAs to the current system. However, these specifications are extremely demanding, and would require a space bandwidth product (SBP) of ~ 991 megapixels (MP), which is far beyond any currently produced objective lenses. **(c)** Another alternative design would maintain the same crossing angles as the current system, instead delivering and collecting all beam paths through a single massive objective lens. The specifications for this objective lens would be even more demanding, with SBP ~ 1351 MP. These alternative designs are highly speculative, and it is not likely that these objective lenses would be technically or financially feasible to design and/or manufacture.

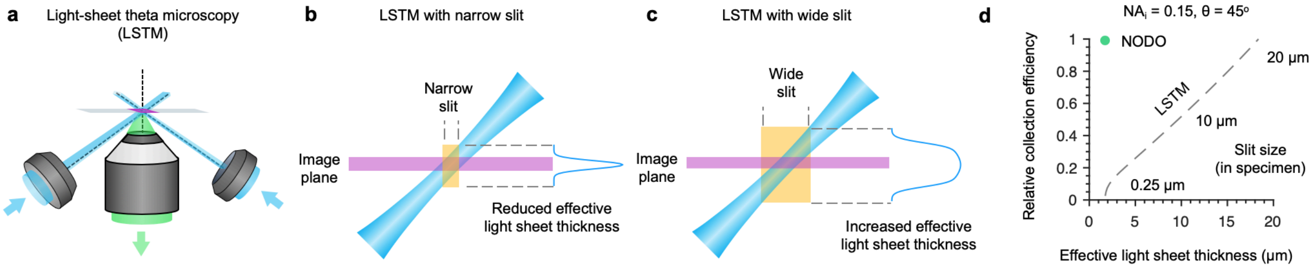

Supplementary Figure 19 | Comparison of light-collection efficiency and effective light-sheet thickness for LSTM and NODO architectures. (a) Rather than using a remote focus to re-image a tilted light sheet, LSTM laterally scans two illuminations beams to generate a virtual light sheet within the specimen that is orthogonal to the collection objective lens. **(b-c)** To reject out-of-focus light, the scanning beams are synced to a confocal slit. A narrow slit maintains a thin effective light-sheet thickness, at the cost of reduced light-collection efficiency. While using a wider slit would increase light efficiency, it would also increase the effective light-sheet thickness due to imaging regions of the light sheet that are outside the image plane (i.e. the focal plane of the collection objective lens). For illustrative purposes, only one of the two illumination beams is shown. **(d)** Simulations were performed comparing NODO and LSTM architectures using the specifications of the current NODO system (NA_i = 0.15 and θ = 45 deg). For the same effective light-sheet thickness, the light-collection efficiency for LSTM is <10% compared to NODO. Likewise, in order to achieve the same light-collection efficiency as NODO, the effective light-sheet thickness for LSTM would be increased from 1.9 µm to 18.4 µm. Therefore, light-collection efficiency and effective light-sheet thickness are inherently coupled for LSTM, whereas they are decoupled for NODO. Note, for NODO imaging, the sCMOS camera is adjusted to match the confocal parameter ($2z_R$) of the Gaussian light sheet, which is ~20 µm.

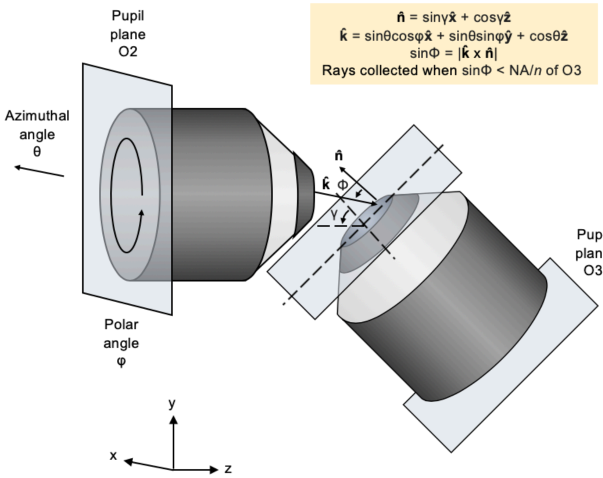

Supplementary Figure 20 | Numerical simulation geometry. Based on a spherical coordinate system, each ray exiting objective lens O2 can be described by an azimuthal angle, θ, and polar angle, φ. The direction of that light ray is then described as $\hat{\mathbf{k}} = \sin\theta\cos\varphi\hat{\mathbf{x}} + \sin\theta\sin\varphi\hat{\mathbf{y}} + \cos\theta\hat{\mathbf{z}}$. The surface normal from objective lens O3 is described by $\hat{\mathbf{n}} = \sin\gamma\hat{\mathbf{x}} + \cos\gamma\hat{\mathbf{z}}$. Therefore, the angle of incidence of the ray on O3 is given by $\sin\Phi = |\hat{\mathbf{k}} \times \hat{\mathbf{n}}|$. The incident pupil plane from O2 can then be clipped by the NA of O3.

References

1. Chung, K., et al., *Structural and molecular interrogation of intact biological systems.* Nature, 2013. **497**(7449): p. 332-7.
2. Tanaka, N., et al., *Whole-tissue biopsy phenotyping of three-dimensional tumours reveals patterns of cancer heterogeneity.* Nature Biomedical Engineering, 2017. **1**(10): p. 796.
3. Susaki, E.A., et al., *Advanced CUBIC protocols for whole-brain and whole-body clearing and imaging.* Nature Protocols, 2015. **10**: p. 1709-1727.
4. Richardson, D.S. and J.W. Lichtman, *Clarifying Tissue Clearing.* Cell, 2015. **162**(2): p. 246-57.
5. Pan, C., et al., *Shrinkage-mediated imaging of entire organs and organisms using uDISCO.* Nat Methods, 2016. **13**(10): p. 859-67.
6. Renier, N., et al., *iDISCO: a simple, rapid method to immunolabel large tissue samples for volume imaging.* Cell, 2014. **159**(4): p. 896-910.
7. Tainaka, K., et al., *Chemical Landscape for Tissue Clearing Based on Hydrophilic Reagents.* Cell Reports, 2018. **24**(8): p. 2196-2210.e9.
8. Susaki, E.A., et al., *Advanced CUBIC protocols for whole-brain and whole-body clearing and imaging.* Nat Protoc, 2015. **10**(11): p. 1709-27.
9. Chung, K. and K. Deisseroth, *CLARITY for mapping the nervous system.* Nat Methods, 2013. **10**(6): p. 508-13.
10. Dodt, H.-U., et al., *Ultramicroscopy: three-dimensional visualization of neuronal networks in the whole mouse brain.* Nature Methods, 2007. **4**(4): p. 331-336.
11. Migliori, B., et al., *Light sheet theta microscopy for rapid high-resolution imaging of large biological samples.* BMC Biology, 2018. **16**(1): p. 57.
12. Tomer, R., et al., *Advanced CLARITY for rapid and high-resolution imaging of intact tissues.* Nature Protocols, 2014. **9**(7): p. 1682-97.
13. Voigt, F.F., et al., *The mesoSPIM initiative: open-source light-sheet microscopes for imaging cleared tissue.* Nature Methods, 2019. **16**(11): p. 1105-1108.
14. Chakraborty, T., et al., *Light-sheet microscopy of cleared tissues with isotropic, subcellular resolution.* Nature Methods, 2019. **16**(11): p. 1109-1113.
15. Glaser, A.K., et al., *Light-sheet microscopy for slide-free non-destructive pathology of large clinical specimens.* Nature Biomedical Engineering, 2017. **1**(7): p. 0084.
16. Barner, L.A., et al., *Solid immersion meniscus lens (SIMlens) for open-top light-sheet microscopy.* Optics Letters, 2019. **44**(18): p. 4451-4454.

17. Glaser, A.K., et al., *Multi-immersion open-top light-sheet microscope for high-throughput imaging of cleared tissues.* Nature Communications, 2019. **10**(1): p. 1-8.

18. McGorty, R., D. Xie, and B. Huang, *High-NA open-top selective-plane illumination microscopy for biological imaging.* Optics Express, 2017. **25**(15): p. 17798-810.

19. McGorty, R., et al., *Open-top selective plane illumination microscope for conventionally mounted specimens.* Optics Express, Vol. 23, Issue 12, pp. 16142-16153, 2015.

20. Strnad, P., et al., *Inverted light-sheet microscope for imaging mouse pre-implantation development.* Nature Methods, 2015. **13**: p. 139-142.

21. Kumar, A., et al., *Dual-view plane illumination microscopy for rapid and spatially isotropic imaging.* Nature Protocols, 2014. **9**: p. 2555-2573.

22. Botcherby, E.J., et al., *An optical technique for remote focusing in microscopy.* Optics Communications, 2008. **281**(4): p. 880-887.

23. Dunsby, C., *Optically sectioned imaging by oblique plane microscopy.* Optics Express, 2008. **16**(25): p. 20306-20316.

24. Voleti, V., et al., *Real-time volumetric microscopy of in vivo dynamics and large-scale samples with SCAPE 2.0.* Nature Methods, 2019. **16**(10): p. 1054-1062.

25. Bouchard, M.B., et al., *Swept confocally-aligned planar excitation (SCAPE) microscopy for high-speed volumetric imaging of behaving organisms.* Nature Photonics, 2015. **9**(2): p. 113-119.

26. Yang, B., et al., *Epi-illumination SPIM for volumetric imaging with high spatial-temporal resolution.* Nature Methods, 2019. **16**(6): p. 501-504.

27. Millett-Sikking, A., et al. *High NA single-objective light-sheet*. 2019; Available from: https://andrewgyork.github.io/high_na_single_objective_lightsheet/index.html.

28. Kumar, M., et al., *Integrated one- and two-photon scanned oblique plane illumination (SOPi) microscopy for rapid volumetric imaging.* Optics Express, 2018. **26**(10): p. 13027-13041.

29. Hoffmann, M. and B. Judkewitz, *Diffractive oblique plane microscopy.* Optica, 2019. **6**(9): p. 5.

30. Yueqian, Z. and G. Herbert, *Systematic design of microscope objectives. Part I: System review and analysis.* Advanced Optical Technologies, 2019. **8**(5): p. 313-347.

31. Dean, K., et al., *Deconvolution-free Subcellular Imaging with Axially Swept Light Sheet Microscopy*, in *Biophys J*. 2015. p. 2807-15.

32. Keller, P.J., et al., *Fast, high-contrast imaging of animal development with scanned light sheet-based structured-illumination microscopy.* Nat Methods, 2010. **7**(8): p. 637-42.

33. Hanser, B.M., et al., *Phase-retrieved pupil functions in wide-field fluorescence microscopy.* Journal of Microscopy, 2004. **216**: p. 16.

34. Van Roey, J., J. van der Donk, and P.E. Lagasse, *Beam-propagation method: analysis and assessment.* Journal of the Optical Society of America, 1981. **71**(7): p. 803-810.